GRIFFITH UNIVERSITY

van der Waals type II carbon nitride homojunctions for visible light photocatalytic hydrogen evolution

Author

Li, Xiaojie, Zhang, Panpan, Zhang, Huayang, Tian, Wenjie, Yang, Yangyang, Hu, Kunsheng, Chen, Dechao, Li, Qin, Duan, Xiaoguang, Sun, Hongqi, Wang, Shaobin

Published

2021

Journal Title

Nano Research

Version

Accepted Manuscript (AM)

DOI

10.1007/s12274-021-3744-x

Rights statement

© 2021 Tsinghua University Press, co-published with Springer-Verlag GmbHs. This is an electronic version of an article published in Nano Research, 2021. Nano Research is available online at: http://link.springer.com// with the open URL of your article.

Downloaded from

http://hdl.handle.net/10072/407131

Griffith Research Online

https://research-repository.griffith.edu.au

TABLE OF CONTENTS (TOC)

van der Waals type II carbon nitride homojunctions for visible light photocatalytic hydrogen evolution

Xiaojie Li[1,2], Panpan Zhang[1], Huayang Zhang[1], Wenjie Tian[1], Yangyang Yang[1], Kunsheng Hu[1], Dechao Chen[3], Qin Li[3], Xiaoguang Duan[1], Hongqi Sun*[4], Shaobin Wang*[1]

[1] School of Chemical Engineering and Advanced Materials, The University of Adelaide, Adelaide, SA 5005, Australia

[2] Department of Chemical Engineering, Curtin University, GPO Box U1987, Perth, WA 6845, Australia

[3] Queensland Micro- and Nanotechnology Centre, School of Engineering and Built Environment, Griffith University, Nathan, QLD 4111, Australia

[4] School of Engineering, Edith Cowan University, Joondalup, WA 6027, Australia

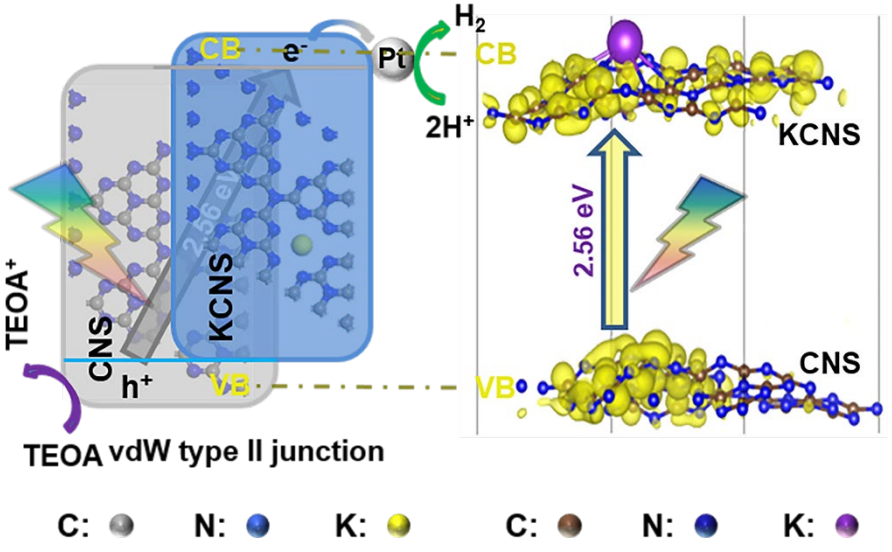

The conduction and valence bands separated in different layers endow van der Waals type II homojunction with excellent electron-hole separation and enhanced photocatalytic hydrogen evolution.

Provide the authors' webside if possible.

Author 1, webside 1

Author 2, webside 2

van der Waals type II carbon nitride homojunctions for visible light photocatalytic hydrogen evolution

Xiaojie Li[1,2], Panpan Zhang[1], Huayang Zhang[1], Wenjie Tian[1], Yangyang Yang[1], Kunsheng Hu[1], Dechao Chen[3], Qin Li[3], Xiaoguang Duan[1], Hongqi Sun[4] (✉), Shaobin Wang[1] (✉)

[1] *School of Chemical Engineering and Advanced Materials, The University of Adelaide, Adelaide, SA 5005, Australia*

[2] *Department of Chemical Engineering, Curtin University, GPO Box U1987, Perth, WA 6845, Australia*

[3] *Queensland Micro- and Nanotechnology Centre, School of Engineering and Built Environment, Griffith University, Nathan, QLD 4111, Australia*

[4] *School of Engineering, Edith Cowan University, Joondalup, WA 6027, Australia*

© Tsinghua University Press and Springer-Verlag GmbH Germany, part of Springer Nature 2018

Received: day month year / **Revised:** day month year / **Accepted:** day month year (automatically inserted by the publisher)

ABSTRACT

Photocatalytic hydrogen evolution reaction (PC-HER) provides a solution to energy crisis and environmental pollution. Herein, different graphitic carbon nitride (g-C_3N_4)-based van der Waals (vdW) type II homojunctions have been fabricated and g-C_3N_4/K-doped g-C_3N_4 nanosheets have an outstanding PC-HER rate of 1243 μmol·h^{-1}·g^{-1} under visible light, higher than that of bulk g-C_3N_4, doped g-C_3N_4 nanosheets, and mixed nanosheets. The enhanced PC-HER performance can be ascribed to the cooperative effects of the shortened bandgap, enlarged specific surface area, matched type II energy band structure, “face to face” vdW charge interaction, and peculiarly partite positions of the conduction and valence bands in different layers. Besides, the type II junctions were found superior to binary type II junction. This study highlights the synergistic effect of different strategies in improving the PC-HER capacities of g-C_3N_4, especially the application of particular vdW junctions, and provides new insights to the structures and mechanism.

KEYWORDS

van der Waals junction; type II junction; hydrogen evolution; carbon nitride; photocatalyst.

1. Introduction

Fossil fuels, including petroleum, coal, natural gas, and shale oil, are currently the primary energy resources for the world [1–3]. However, those non-renewable energy resources will run out in the next ~ 200 years [4–6], and the combustion products, e.g. CO_2, and trace amounts of SO_2 and NO_2, not to say methane itself, can lead to greenhouse effects [7, 8] and environmental pollution [9, 10]. Thus, clean energy is urgently required for the sustainable human development. Photocatalytic hydrogen evolution reaction (PC-HER), with the merits in the reproducibility and cleanliness of H_2, and the environmental friendliness of PC-HER processes, offers a promising solution to the above issues [11–13].

In 2009, Wang et al. for the first time employed graphitic carbon

Address correspondence to First A. Firstauthor, email1; Third C. Thirdauthor, email2

nitride (g-C_3N_4) as the photocatalyst in a PC-HER system [14], thereafter, this material promptly became a superstar in photocatalysis owing to its easy preparation, suitable bandgap, non-toxicity, physicochemical firmness, and non-metal nature [15–18]. A large number of measures have been designed and exploited to continually advance its PC-HER to a higher level in the past decade. For example, exfoliating bulk g-C_3N_4 into nanosheets can remarkably enlarge the specific surface area and provide more active sites [19, 20]. Doping heteroatoms to the g-C_3N_4 framework can optimize its properties, for instance, increasing its optical absorption, tuning its bandgap, modifying its electrical conductivity, and shifting its HOMO-LUMO levels [21, 22]. Besides, type II junctions, formed by the connection of two semiconductors with a staggered band structure, can impede the reintegration of photo-motivated charges of both the two materials by transferring photoelectrons and holes from each other [23, 24]. What is more, van der Waals (vdW) junctions, composed of several two-dimensional (2D) materials with a "face to face" contact, are gaining great attention in recent years due to their marvelous properties benefiting from the electronic interactions via massive intimate interfaces [25, 26].

Thus, combining all those four strategies into one material can collectively integrate all their advantages to boost the PC-HER process. Herein, g-C_3N_4 self-based vdW type II and binary type II junctions were obtained via a thermal doping and co-exfoliation method. Specifically, the structured hybrids include g-C_3N_4/B-doped g-C_3N_4 nanosheets (CN-BCN-S), g-C_3N_4/K-doped g-C_3N_4 nanosheets (CN-KCN-S), B-doped g-C_3N_4/K-doped g-C_3N_4 nanosheets (BCN-KCN-S), and g-C_3N_4/B-doped g-C_3N_4/K-doped g-C_3N_4 nanosheets (CN-BCN-KCN-S, binary type II). Their enhanced PC-HER performances were ascribed to the synergistic effects of shortened bandgaps, enlarged specific surface areas, matched energy band structures, "face to face" charge transfers, and more significantly, the location of the conduction and valence bands in different layers. Moreover, this study, for the first time, discusses the mechanism of carbon nitride type II junctions in favor to binary type II junctions.

2. Experimental

2.1. Chemicals and materials

Urea, boric acid, potassium hydroxide, sodium sulfate, triethanolamine, chloroplatinic acid, and Nafion solution were ordered from Sigma-Aldrich. All the chemicals are ACS reagents and utilized without further purification.

2.2. Preparation of catalysts

Synthesis of g-C_3N_4: 10 g urea was put in a crucible, which was then covered with a lid and transferred in a muffle furnace. The temperature was kept at 550 °C for 4 h with a heat-up rate of 15 °C/min. The obtained bulk g-C_3N_4 was pulverized in a hard plastic container with a stirrer bar by a vortex mixer. The prepared powder was denoted as CN.

Fabrication of B-doped g-C_3N_4 (or K-doped g-C_3N_4): 10 g urea and 3 mg boric acid (or 10 mg potassium hydroxide) were dissolved in 12 mL ultrapure water in a crucible. The mixture was stirred homogeneously, dried at 100 °C and then transferred into a muffle furnace with a lid. The temperature was kept at 550 °C for 4 h with a heat-up rate of 15 °C/min. The acquired bulk solid was pulverized and then rinsed with ultrapure water and ethanol several times by filtration and dried at 100 °C. The obtained materials were ground again and denoted as BCN (or KCN).

Preparation of B, K co-doped g-C_3N_4: 10 g urea, 3 mg boric acid, and 10 mg potassium hydroxide were dissolved in 12 mL ultrapure water in a crucible. With the similar thermal treatment as above, the acquired bulk particles were still white crystal, same as the state before polymerization. This is because of the reaction of boric acid and potassium hydroxide in the dissolving and drying processes. The produced potassium metaborate with a boiling point at 1401 °C would thoroughly mix with urea and protect the urea from being polymerized.

Fabrication of g-C_3N_4 nanosheets (or B-doped g-C_3N_4 nanosheets, or K doped g-C_3N_4 nanosheets): 480 mg CN (BCN or KCN) was put in a crucible with a lid, which was then transferred in a muffle furnace. The temperature was kept at 500 °C for 4 h with a heat-up rate of 15 °C/min. The obtained powder was denoted as CNS (or BCNS, or KCNS, accordingly).

Preparation of a binary mixture of CNS and BCNS (or a mixture of CNS and KCNS, or a mixture of BCNS and KCNS): 120 mg CNS and 120 mg BCNS (or 120 mg CNS and 120 mg KCNS, or 120 mg BCNS and 120 mg KCNS) were thoroughly mixed in a hard plastic container with a stirrer bar by a vortex mixer. The obtained mixture was denoted as CNS-BCNS (or CNS-KCNS, or BCNS-KCNS).

Preparation of the ternary mixture of CNS, BCNS and KCNS: 80 mg CNS, 80 mg BCNS, and 80 mg KCNS were fully mixed in a hard plastic container with a stirrer bar by a vortex mixer. The obtained mixture was denoted as CNS-BCNS-KCNS.

Fabrication of g-C_3N_4/B-doped g-C_3N_4 (or g-C_3N_4/K-doped g-C_3N_4, or B-doped g-C_3N_4/K-doped g-C_3N_4) nanosheets-based van der Waals type II homojunction: 240 mg CN and 240 mg BCN (or 240 mg CN and 240 mg KCN, or 240 mg BCN and 240 mg KCN) were thoroughly mixed in a hard plastic container with a stirrer bar by a vortex mixer. The mixture was then shifted in a muffle furnace, and the temperature was kept at 500 °C for 4 h with a heat-up rate of 15 °C/min. The obtained powder was denoted as CN-BCN-S (or CN-KCN-S, or BCN-KCN-S).

Fabrication of g-C_3N_4/B-doped g-C_3N_4/K-doped g-C_3N_4 nanosheets-based van der Waals binary type II junction: 160 mg CN, 160 mg BCN, and 160 mg KCN were thoroughly mixed in a hard plastic container with a stirrer bar by a vortex mixer. The mixture was then thermally treated as the above-mentioned procedure. The obtained powder was denoted as CN-BCN-KCN-S.

2.3. Characterization of the materials

Scanning electron microscopy (SEM) was achieved using a JEOL JSM-7800F & TEAM Octane Plus microscope (Japan). Atomic force microscopy (AFM) was realized via a XE-100 microscope (Park Systems, USA). Transmission electron microscopy (TEM) and electron energy-loss spectroscopy (EELS) were acquired from an FEI Titan Themis 80-200 microscope (USA) at 80 kV. The energy dispersive X-ray spectroscopy (EDS) elemental mapping was carried out through a JEOL F200 microscope (Japan). X-ray diffraction (XRD) patterns were obtained using a powder X-ray diffractometer at 40 kV and 15 mA with Cu Kα radiation (Miniflex,

Rigaku). X-ray photoelectron spectroscopy (XPS) was conducted on an Axis Ultra (Kratos Analytical, UK) XPS spectrometer assembled with an Al Kα source (1486.6 eV). Near-edge X-ray absorption fine structure (NEXAFS) data were obtained at the wiggler X-ray absorption structure (XAS) Beamline (12ID) at the Australian Synchrotron in Melbourne. Nitrogen adsorption and desorption isotherms were measured on a MicrotracBEL max (Japan) to analyze the specific surface area. UV-vis diffuse reflectance spectra were performed on a Cary 100 UV-Vis spectrophotometer (Agilent, USA) with $BaSO_4$ as the reference sample. Photoluminescence (PL) spectra of the samples were recorded on an F4700 Hitachi (Japan).

2.4. Photoelectrochemical tests

A Zennium electrochemical workstation (Zahner, Germany) was utilized for Mott-Schottky tests under a typical three-electrode system, and the electrolyte was a Na_2SO_4 solution (0.05 M pH = 6.8). A platinum sheet and a Ag/AgCl electrode served as the counter and reference electrodes, respectively. The sample membrane loaded on a fluorine-doped tin oxide (FTO) glass was the working electrode. In detail, a catalyst (5 mg), absolute ethanol (1 mL), and Nafion solution (10 μL) were mingled together homogeneously. The acquired suspension was spin-coated onto the FTO glass, and the synthesized electrode was desiccated at 100 °C overnight. The loading amount of the catalyst was about 0.60 $mg \cdot cm^{-2}$.

2.5. Photocatalytic measurements

Photocatalytic hydrogen evolution measurements were performed in a black Teflon cell with a quartz light window. The light source was a 300 W Xenon lamp (Newport) with a UV cut-off filter ($\lambda > 420$ nm). In a typical experiment, 20 mg photocatalysts were added in a mixed solution of 90 mL ultrapure water and 10 mL triethanolamine (TEOA), followed by injecting 120 μL H_4PtCl aqueous solution (5 mg Pt/mL) to the mixed solution to provide 3 wt% Pt co-catalysts. After 5-minute ultrasonication, the mixed suspension was transferred in the reactor, which was then sealed tightly. Nitrogen gas was utilized to purge the air in the reactor and the reaction solution for 30 min with vigorous stirring, and then the light source was switched on to start the reactions. Meanwhile, the temperature of the reaction system was kept at 25 °C with a water circulation system. The generated hydrogen was online examined by a 490 Micro GC (Agilent, USA) equipped with a thermal conductivity detector. A narrow-band-pass filter (420 nm) was exploited for the apparent quantum efficiency (QE). The illuminator intensity was measured with a 340 solar meter (OAI, USA). The QE was evaluated using the equation below.

QE% = number of reacted electrons/number of incident photons *100 = number of evolved H_2 molecules *2/number of incident photons * 100 (1)

2.6. Theoretical methodology

All the calculations were conducted by applying the Vienna Ab initio Simulation Package (VASP) [27, 28]. The ion-electron interaction and the electron exchange-correction energy were described by using the projected augmented wave method and the generalized gradient approximation of the Perdew−Burke−Ernzerhof (PBE), respectively [29]. A 400 eV cut-off energy was used in the simulation. All the atomic positions and lattice parameters were optimized during the structural relaxation via the conjugate gradient algorithm. The simulations did not stop until the residual forces on constituent atoms were less than 0.03 eV/Å. The 2×2×1 and 3×3×1 k-grids were applied in structural optimization and calculations of electronic properties, respectively. Besides, the van der Waals interactions were also figured by using the DFT-D3 method of Grimme [30]. The visualization of charge distribution was realized by using the VESTA program [31].

3. Results and discussions

3.1. Heteroatom doping

The fabrication of vdW type II and binary type II junctions was conducted through a thermal co-exfoliation strategy with CN, BCN, and KCN as the precursors, which were synthesized via thermal polymerization. Thus, we firstly conducted XPS to confirm the successful doping of B for BCN and K for KCN. As shown in Fig. S1(a), the main C 1s peak of BCN at 288.0 eV is the result of sp^2 carbon jointed to the three nitrogen atoms ($C-(N)_3$) in the g-C_3N_4 grid. The other C 1s peak is from the unavoidably adventitious graphitic carbon atoms (C-C). The N 1s peak at 398.5 eV of BCN (Fig. S1(b)) accords with the sp^2-bonded N atoms in the graphite-like g-C_3N_4 framework (C−N=C). The peak of 399.8 eV results from the nitrogen ternary groups ($N-(C)_3$) or H–N–$(C)_2$, while the peak at 401.2 eV signifies the N in the center of heptazine rings. Lastly, the one at 404.4 eV signifies the characteristic π-excitation [32–35]. B 1s peak of BCN is clearly shown at 191.5 eV in Fig. S1(c), denoting the success of boron doping in BCN. The C 1s (Fig. S2(a)) and N 1s (Fig. S2(b)) spectra of KCN show no significant difference with those of BCN. The two K 2p peaks at 296.1 and 294.4 eV refer to K $2p_{1/2}$ and K $2p_{3/2}$, respectively (Fig. S2(c)), proving the successful loading of potassium in KCN [36, 37].

According to previous reports, for B-doped g-C_3N_4, boron atoms are inclined to substitute carbon atoms [38] (Scheme S1A) (denoted as BCN-C) or the N atoms connected with three tri-s-triazine moieties [39] (Scheme S1B) (denoted as BCN-N) in the framework of g-C_3N_4, while for K-doped g-C_3N_4, potassium atoms are apt to be trapped in the six-fold cavity of the g-C_3N_4 structure (Scheme S1C) [40]. To identify the B loading position of BCN in this study, we analyzed the data of DFT calculations and NEXAFS. When comparing the sum of valence electrons (SVE) of carbon atoms in CN and BCN-C (Fig. S3 and S4, Table S1), we can find that the carbon SVE of BCN-C is much lower than that of CN, indicating fewer electrons accumulated on carbon atoms in BCN-C. This is because one C atom is replaced by a B atom in the model of BCN-C, as shown in Fig. S4. From Table S1, we can also find that BCN-C has a higher value than CN for the SVE of pyridinic N and the graphitic N connected with three tri-s-triazine moieties (GNTT), indicating that more electrons are gathered on the pyridinic N and GNTT in BCN-C. In contrast, BCN-N owns higher SVE in carbon atoms and lower SVE in pyridinic N and GNTT than those of CN (Fig. S3 and S5, Table S1). Since one-layer models are utilized for the calculations, we analyzed the NEXAFS of BCNS and CNS with fewer layers, instead of CN and BCN with a bulk structure. Fig. S6(a) shows that the peak of BCNS for C-N=C has a significant red shift compared to that of CNS, meaning that fewer electrons are gained by carbon atoms in BCNS than in CNS. Besides, both the peaks of pyridinic N and GNTT of BCNS have blue shifts than CNS (Fig. S6(b)), forecasting that the electrons on pyridinic N and GNTT of BCNS are more than that of CNS. Consequently, it can be derived that the NEXAFS data of BCNS are consistent well with the BCN-C structure in the DFT calculations. It is then concluded that B is substituting C in BCNS

in this study. After that, we employed the similar strategy to confirm that K is locating at the six-fold cavity of CNS to form KCNS (Table S1, Fig. S3, S7 and S8). Specifically, we first compared the carbon SVE of CN and KCN (K occupies the six-fold cavity). It can be found from table S1, Fig. S3 and S7, that the carbon SVE of KCN is slightly higher than that of CN, indicating that the carbon atoms of KCN have more charges accumulated compared to that of CN. Meanwhile, from Fig. S8(a), it can be seen that the main peak of C K-edge of KCNS is left-shifted compared to CNS, also showing that the charge of C of KCNS is more than that of CNS. Besides, in Table S1, the SVE of pyridine N and GNTT of KCN is higher than that of the corresponding N of CN, proving that the pyridine N and GNTT of KCN have more charges than the corresponding N of CN. In Fig. S8(b), the two peaks of N K-edge of KCNS are blue-shifted than CNS, presenting that the two kinds of N of KCNS are more charged than that of CNS, in accordance with the SVE result of DFT calculation. Based on all these analyses, it can be demonstrated that the structure of KCN in DFT calculation is consistent with the structure of KCNS. In addition, B K-edge peaks (Fig. S6(c)) and K L-edge peaks (Fig. S8(c)) can complementally prove the success of B doping in BCNS and K doping in KCNS.

3.2 Van der Waals junctions

After the demonstration of the doping and the structure of BCN and KCN, we take CN-KCN-S as an example for the vdW type II junction. Firstly, in the SEM image of CN-KCN-S (Fig. S9), a large number of lamellae and lamella stacks can be seen in the material structure. Besides, AFM image (Fig. S10) shows that there exists a stack of two-layer flakes, and the thickness of each flake is about 3 nm. As a result, it is possible to find the van der Waals type II junctions formed by CNS and KCNS in those stacks observed from SEM and AFM images. Thus, we further use TEM to investigate the morphology of CN-KCN-S. As shown in Fig. 1(a), two pieces of two-dimensional (2D) layers are stacked together with an extensive interface. In each of the two slices, a small area is selected for EELS scanning. As shown in Fig. 1(b), C K-edge and N K-edge peaks exist for Area 1. In contrast, a peak of K L_2-edge emerges for Area 2 as compared to Area 1. Those results reveal that the sheet located by area 1 is CNS, while the other sheet with area 2 is KCNS. In addition, the EDS mapping images (Fig. S11) also show that in CN-KCN-S, there exist layer stacks where the upper layer containing K element is KCNS, while the lower layer not containing K is CNS. Consequently, the CN-KCN-S vdW junction is preliminarily verified.

XRD is then explored to compare the different crystal phases among all the samples. The (100) peak at ~ 13.0° (Fig. S12(a)) is owing to the ordering of tri-s-triazine units at 0.675 nm within a g-C_3N_4 plane, while the (002) peak at about 27.5° denotes the interlayer piling of the conjugated double bonds for graphitic materials, consistent with previously reported 0.33 nm of interlayer spacing [22, 41–43]. From all the patterns in Fig. S12, we can observe that the (002) peak of nanosheets has a minor right-shift compared to the bulk counterparts, indicating a narrowed interlayer distance, which is consistent with the data from the literature [44, 45]. Fig. S13 illustrates the XRD patterns of boron and potassium doped g-C_3N_4. The bulk samples (Fig. S13(a)) show that both boron doping and potassium doping can make a left shift of the (002) peak, indicating a widened layer-to-layer space due to the larger atom radii of B and K than those of C and N. A similar trend of doping effect is displayed in the nanosheet samples (Fig. S13(b)). The smaller changes between doped CNS and pure CNS compared to the bulk group should be ascribed to the right shift of the nanosheets, as explained in Fig. S12.

A comprehensive XRD study on vdW type II and binary type II junctions, mixtures of counterparts, and the corresponding nanosheets is reflected in Fig. 2. Comparison of CNS, BCNS, and the vdW type II junction of CN-BCN-S (Fig. 2(a)) exhibits a left offset in the (002) peak, which may be the result of that the distance between CNS and BCNS layers is slightly wider than the interspace of CNS or BCNS themselves because of the weak vdW interaction of hetero layers. The mixture of CNS-BCNS also shows a minor left shift in the (002) peak, but it is not so significant as the change of CN-BCN-S. This indicates that minor vdW junctions might also be formed in CNS-BCNS, but they are inefficient as compared to CN-BCN-S vdW junction. Similar tendencies can be found in CN-KCN-S (Fig. 2(b)) and BCN-KCN-S type II vdW junctions (Fig. 2(c)), as well as CN-BCN-KCN-S binary type II vdW junction (Fig. 2(d)).

Fig. S14 compares the NEXAFS spectra of C, N K-edge of vdW type II junctions and their corresponding nanosheets. From the data, it can be seen that the number and shape of the C and N peaks of all the samples are basically similar, and specially, the C and N peaks of all van der Waals Type II junctions are located in the middle of those peaks of their corresponding nanosheets. The observations indicate that, in the as-fabricated vdW nanostructures, vdW forces are the mainstay and no obvious covalent bond exists in the structures. All the above characterizations demonstrated the successful fabrication of a series of g-C_3N_4 self-based vdW junctions, thereafter, we further explored their energy band structures.

3.3 Type II junctions

UV-vis diffuse reflectance spectra (DRS) were acquired to investigate the optical properties of the as-fabricated materials. Fig. S15 compares the spectra of nanosheets and bulk counterparts, and suggests that all the nanosheets have a bit weak UV absorption. Besides, only KCNS can show an obvious increase in the range of 450 – 800 nm compared to its bulk counterpart (KCN). After the thermal exfoliation, more potassium atoms can be exposed on the surface of KCNS. As a metal element, potassium atoms can help improve visible light absorption [37, 46]. The bandgap energies (Fig. S15(d-f)) were then determined from the UV-vis diffuse reflectance data via the Kubelka-Munk equation of $(\alpha h\nu)^n = k(h\nu - \mathrm{Eg})$ (where α, ν, k, and Eg stand for the absorption factor, optical frequency, proportionality constant, and bandgap energy, respectively; $n = 2$ for direct bandgap semiconductors and $n = 1/2$ for indirect bandgap semiconductors) [47]. The widened bandgaps of nanosheets in comparison with bulk counterparts are consistent with previously reported data [19, 48, 49]. Fig. 3 displays that the optical absorption intensity of these materials follows an order of KCN > BCN > CN and KCNS > BCNS > CNS and that their bandgap energies are in an order of KCN (2.50 eV) < BCN (2.52 eV) < CN (2.58 eV) and KCNS (2.52 eV) < BCNS (2.56 eV) < CNS (2.65 eV). It can be seen that the bandgap differences are enlarged in the nanosheet materials.

As for vdW type II junctions (Fig. S16), binary mixtures (Fig. S17), vdW binary type II junction (Fig. S18(a) and (c)), and the ternary mixture (Fig. S18(b) and (d)), their absorption intensity and bandgap energy are among their matching nanosheet materials.

Mott-Schottky (MS) tests were conducted to further determine their band structures. As presented in Fig. 4 and Fig. S19-22, the tangent slopes of all curves are positive, manifesting that all the as-synthesized materials are n-type semiconductors. The intercept of the plot tangent and the X-axis in MS can reflect the flat band position of the materials. For n-type semiconductors, this value can be approximately viewed as the conduction band (CB) position. Fig. S19 makes it clear that the CB values of nanosheets are more negative than those of bulk counterparts. Fig. 4(a) shows that the CB order is KCN (-1.04 V vs Ag/AgCl, pH = 6.8) < BCN (-0.93 V) < CN (-0.92 V). Moreover, the differences in nanosheets group are more significant (Fig. 4(b)), showing KCNS (-1.17 V) < BCNS (-1.03 V) < CNS (-0.95 V). The vdW type II junctions (Fig. S20) and the binary mixtures (Fig. S21) have CB positions in between those of their matching nanosheets materials. Fig. S22 exposes that the vdW binary type II junction and the ternary mixture also own CB values among their corresponding nanosheets semiconductors.

Based on the above UV-vis DRS and MS data, the energy band structures of nanosheets and bulk g-C_3N_4 based semiconductors are shown in Fig. 5(a). The CNS has a widened bandgap compared to CN, with a more negative CB while more positive VB positions. Unlike CNS, although BCNS and KCNS have wider bandgap energies than their bulk counterparts, while their CB and VB values are more negative than their matching counterparts. Besides that, from CNS to BCNS and then to KCNS, the bandgaps are gradually diminishing (2.65, 2.56, and 2.52 eV), and both the CB (-0.95, -1.03, -1.17 V vs Ag/AgCl, pH = 6.8) and VB (1.70, 1.53, 1.35 V vs Ag/AgCl, pH = 6.8) are decreasing accordingly. These results fully manifest that perfect type II junctions can be formed between any two of them, and excellent binary type II junction can also be obtained by their combination. We calculated the energy structures of vdW type II junctions based on the experimental results (Fig. S16, S18(c), S20, and S22). Fig. 5(b) shows that all the CB, VB, and bandgap values of vdW type II junctions are in between those of their corresponding nanosheets (Fig. 5(a)).

3.4. Characterizations and PC-HER performances

N_2 adsorption-desorption isotherms were then tested to obtain the specific surface area (SSA) of the samples. Fig. S23 and Table S2 suggest that the SSA of nanosheets is about 1.5 - 2 times larger than that of their bulk counterparts. The larger SSA will provide more active sites for photocatalysis, and the thinner nanosheet will also facilitate the migration of photogenerated electrons in the inner layer of the surface. However, the SSA of doped g-C_3N_4 is decreased after doping compared to pure g-C_3N_4. Although vdW type II junctions do not have a larger SSA than their corresponding nanosheets, they still have some advantages over their bulk precursors. The SSA of the mixture of nanosheets is between the two precursor nanosheets, which might be due to that simple mixing cannot effectively help form a heterojunction.

PL was carried out to probe the separation, transfer, and reintegration of charge carriers in the samples. From Fig. S24, it is unexpectedly found that the PL intensity of nanosheets is higher than that of their bulk counterparts. This could be because the emerged defects of nanosheets from the thermal exfoliation process may become the recombination centers of photoelectrons and holes. However, this shortcoming of nanosheets cannot conceal the advantage of the large specific surface area of the nanosheets, which will be later discussed in the PC-HER performance. Fig. S25 shows that both B doping and K doping can reduce the PL intensity, possibly due to the introduction of intermediate energy bands [50] or the improvement of electrical conductivity. More importantly, van der Waals type II junctions (Fig. 6(a-c)) have smaller PL intensities than their corresponding nanosheets, convincingly confirming that the type II junction in the large van der Waals interface can forcefully suppress the recombination of photogenerated charges. In comparison, Fig. 6(d-f) show that, for the mixture of nanosheets, PL intensities are only between their two nanosheet sources, indicating that the vdW type II junction cannot be effectively formed by the merely mechanical mixing. This highlights the significance of thermal co-exfoliation in the preparation of vdW type II junction from the preparation aspect.

PC-HER measurements were conducted to evaluate the PC-HER efficiencies of the samples (Fig. 7). In the bulk group, both boron and potassium doping can help improve the PC-HER efficiency of g-C_3N_4, mainly resulting from the decreased bandgap (Fig. 5), increased light absorption (Fig. 3) and reduced combination of charge carriers (Fig. S25) of BCN and KCN than those of CN. The nanosheet group has a remarkably enhanced PC-HER performance compared to the bulk group; however, their PC-HER rate order is KCNS > CNS > BCNS, which is different from the order of KCN > BCN > CN in the bulk samples. Besides, from CN to CNS, the PC-HER rates are increased by a factor that is significantly greater than that of BCN to BCNS and KCN to KCNS. These phenomena may be due to the fact that part of the C and N volatilize in the form of CO_2 and NH_3 during the thermal-exfoliation process, while B and K are not easy to volatize. As a result, the content of B and K will increase and even exceed the optimal value in the BCNS and KCNS, which is not conducive to PC-HER performances.

Besides, all the mixtures, including binary mixtures and the ternary mixture of CNS-BCNS-KCNS, have slightly better PC-HER efficiency than that of the nanosheets. This is probably because some junctions may be formed in these mixtures at a lower level under stirring in the photocatalytic process, leading to the mitigated reintegration of photogenerated electrons and holes. However, no apparent regularity can be found among those mixtures, maybe resulting from their randomly formed minor heterojunctions. The vdW junction group contains three vdW type II junctions and one vdW binary type II junction. The vdW type II junctions own significantly superior PC-HER rates to all the other g-C_3N_4 based materials. This is because of the synergistic effect of enhanced light absorption (heteroatom doping effect), enlarged specific surface area (nanosheet effect), improved charge transfer (type II junction effect), and the vast interface interaction (vdW junction effect). Among those three vdW type II junctions, CN-KCN-S presents the best PC-HER capacity of 1243 $\mu mol \cdot h^{-1} \cdot g^{-1}$, 1.1- and 1.3-fold higher than that of CN-BCN-S and BCN-KCN-S, respectively (1.5 times that of CNS and KCNS, and 8.9 times that of CN). It is also among the top values of doped g-C_3N_4 based materials (Table S3), with the apparent quantum efficiency of 1.7%. As displayed in Fig. 5 and Scheme S2, the more powerful charge-transfer driving force of CN-KCN-S ($|CB_{KCNS} - CB_{CNS}| > |CB_{KCNS} - CB_{BCNS}|$; $|CB_{KCNS} - CB_{CNS}| > |CB_{BCNS} - CB_{CNS}|$; $|VB_{KCNS} - VB_{CNS}| > |VB_{KCNS} - VB_{BCNS}|$; $|VB_{KCNS} - VB_{CNS}| > |VB_{BCNS} - VB_{CNS}|$) can account for its superiority than CN-BCN-S and BCN-KCN-S.

The prominent stability of CN-KCN-S is also evidenced by 3 cycles of a 4-h photocatalytic test as manifested in Fig. S26. Additionally, Fig. S27 and S28 show that, the XRD 002 peak of the catalyst before and after PC-HER test does not have significant shift, and the morphology of the catalyst does not change distinctly, indicating that the catalyst is stable in structure before and after the reaction. Moreover, we also tried to exploit the same fabrication route to prepare boron and potassium co-doped g-C_3N_4 to compare with BCN-KCN-S. However, the trial failed as described in the part of the fabrication of photocatalysts because the produced potassium metaborate with the boiling point at 1401 °C would prevent the urea from being polymerized. This reflects the flexibility of our synthesis approach from another point of view. More critically, the PC-HER rates of all three vdW type II junctions unexpectedly surpass that of the vdW binary type II junction, which is in accord with the PL results (Fig. 8(a)), presumably originating from the structure of vdW binary type II junction. As depicted in Fig. 8(b), after the first-step charge transfer (photoelectrons transfer from KCNS to BCNS, photogenerated holes transfer from CNS to BCNS), and before the second-step charge transfer (photoelectrons transfer from BCNS to CNS, photogenerated holes transfer from BCNS to KCNS), the middle semiconductor (BCNS) can become the recombination center of photo-motivated electrons and holes.

3.5. Catalytic Mechanism

To better illustrate the energy-band differences between pure g-C_3N_4 and g-C_3N_4 self-based vdW type II junction, we used a two-layer model to study the position of the conduction and valence bands of CNS and CN-KCN-S vdW type II junction. As described in Fig. 9(a) and (b), in pure two-layer CNS (2CNS), the states of valence band maximum (VBM) are mainly distributed on the top of N atoms, while the states of conduction band minimum (CBM) are localized on C atoms. It should be emphasized that no difference of VBM and CBM positions between these two layers exists. However, in the model of CN-KCN-S, the VBM states are mainly confined on the top of C and N atoms in the bottom CNS layer, with a slight charge distributed on the top KCNS layer (Fig. 9(c)). In contrast, the CBM states localize on the top KCNS layer (Fig. 9(d)). The large spatial distances of separated photoelectrons and holes in different layers are helpful to elongate the lifetime of photo charges, and favorable to PC-HER processes.

Based on all the above analysis, different from the traditional principle (Scheme S2), a new mechanism for the best candidate of vdW type II junctions, CN-KCN-S, was proposed in Scheme 1. When CN-KCN-S vdW type II junction is formed, the CBM and VBM are separated in different layers (CBM in KCNS: -1.02 V vs Ag/AgCl, and VBM in CNS: 1.54 V vs. Ag/AgCl; Fig. 5(b)), and the bandgap becomes 2.56 eV (Fig. S16(e) and Fig. 5(b)). Under visible light irradiations (> 420 nm), photoelectrons are excited and mostly would then jump from CNS to KCNS via their vast “face to face” vdW contact, while the holes are left in CNS. The recombination of photo charges can then be efficiently suppressed by the cross-layer spatial distance between CB and VB positions. Then the photoelectrons flow to the platinum co-catalyst and react with hydrogen ions from the water on the surface of platinum nanoparticles, after which, hydrogen molecules are generated. Simultaneously, the photo-motivated holes on CNS are consumed by the sacrificial agent of TEOA. Herein, all the factors, including the co-catalyst, sacrificial agent, shortened bandgap of CN-KCN-S than that of CNS, large specific surface area of the nanosheets, vast “face to face” vdW contact, and especially the cross-layer split VB and CB positions, are synergistically contributing to the PC-HER process.

4. Conclusion

In this work, g-C_3N_4 self-based vdW type II homojunctions were prepared through a facile co-thermal-exfoliation method with g-C_3N_4 and heteroatom doped g-C_3N_4 as the precursors. The structures of the doped precursors were demonstrated to be that B substitutes some C atoms for BCN and that K is located in the six-fold cavity of CN for KCN. The vdW type II homojunctions show reduced PL intensity than their two corresponding nanosheets, while the mixture of nanosheets only have PL intensity between their corresponding nanosheets. In the visible light driven PC-HER processes, vdW type II homojunctions outperformed mixtures, nanosheets, doped and undoped bulk CN. Specially, the best performance of the CN-KCN-S could be ascribed to the synergistic effect of shortened bandgaps of KCNS than that of CNS, enlarged specific surface area, matched type II energy band structure, “face to face” vdW charge interaction, and notably the divided CB and VB positions in KCNS and CNS layers, respectively. What is more, the type II junctions were found superior to the binary type II junction, and the drawback of the binary type II junction is the generation of a middle semiconductor as the reintegration center of photogenerated electron and hole pairs. This study discloses the cooperative effect of different strategies in enhancing the PC-HER capacities of g-C_3N_4, especially the construction of vdW junctions and application, and provides some new insights in homojunction system for photocatalysis.

Acknowledgements

X.L. and P.Z. contributed equally to this work. This work was financially supported by the Australian Research Council (DP170104264). The authors acknowledge the technical supports from the Australian Synchrotron, Victoria, Australia, part of ANSTO. The simulations were performed on resources provided by the Pawsey Supercomputing Centre with funding from the Australian Government and the Government of Western Australia.

Electronic Supplementary Material: Supplementary material (Tables S1-3, Schemes S1-2, and Figs. S1–S28, including the supplementary data of XRD, XPS, NEXAFS, UV-vis, SEM, AFM, etc.) is available in the online version of this article at http://dx.doi.org/10.1007/s12274-***-****-*.

References

[1] Höök, M.; Tang, X. Depletion of Fossil Fuels and Anthropogenic Climate Change-A Review. *Energy Policy* **2013**, *52*, 797–809.

[2] Shaffer, G.; Olsen, S. M.; Pedersen, J. O. P. Long-Term Ocean Oxygen Depletion in Response to Carbon Dioxide Emissions from Fossil Fuels. *Nat. Geosci.* **2009**, *2* (2), 105–109.

[3] York, R. Do Alternative Energy Sources Displace Fossil Fuels? *Nat. Clim. Chang.* **2012**, *2* (6), 441–443.

[4] Tollefson, J. Energy Crisis Upsets Platinum Market. *Nature* **2008**, *451* (7181), 877.

[5] Dalton, R. Californian Labs Feel the Heat of Energy Crisis. *Nature* **2001**, *411* (6835), 227.

[6] Qureshi, M. I.; Rasli, A. M.; Zaman, K. Energy Crisis, Greenhouse Gas Emissions and Sectoral Growth Reforms: Repairing the Fabricated Mosaic. *J. Clean. Prod.* **2016**, *112*, 3657–3666.

[7] Worden, H. M.; Bowman, K. W.; Worden, J. R.; Eldering, A.; Beer, R. Satellite Measurements of the Clear-Sky Greenhouse Effect from Tropospheric Ozone. *Nat. Geosci.* **2008**, *1* (5), 305–308.

[8] Qiao, H.; Zheng, F.; Jiang, H.; Dong, K. The Greenhouse Effect of the Agriculture-Economic Growth-Renewable Energy Nexus: Evidence from G20 Countries. *Sci. Total Environ.* **2019**, *671*, 722–731.

[9] Mamba, G.; Mishra, A. K. Graphitic Carbon Nitride ($g\text{-}C_3N_4$) Nanocomposites: A New and Exciting Generation of Visible Light Driven Photocatalysts for Environmental Pollution Remediation. *Appl. Catal. B Environ.* **2016**, *198*, 347–377.

[10] Ren, X.; Chen, C.; Nagatsu, M.; Wang, X. Carbon Nanotubes as Adsorbents in Environmental Pollution Management: A Review. *Chem. Eng. J.* **2011**, *170* (2–3), 395–410.

[11] Wang, W.; An, T.; Li, G.; Xia, D.; Zhao, H.; Yu, J. C.; Wong, P. K. Earth-Abundant $Ni_2P/g\text{-}C_3N_4$ Lamellar Nanohydrids for Enhanced Photocatalytic Hydrogen Evolution and Bacterial Inactivation under Visible Light Irradiation. *Appl. Catal. B Environ.* **2017**, *217*, 570–580.

[12] Li, J.; Shen, B.; Hong, Z.; Lin, B.; Gao, B.; Chen, Y. A Facile Approach to Synthesize Novel Oxygen-Doped $g\text{-}C_3N_4$ with Superior Visible-Light Photoreactivity. *Chem. Commun.* **2012**, *48* (98), 12017–12019.

[13] Zeng, D.; Zhou, T.; Ong, W. J.; Wu, M.; Duan, X.; Xu, W.; Chen, Y.; Zhu, Y. A.; Peng, D. L. Sub-5 Nm Ultra-Fine FeP Nanodots as Efficient Co-Catalysts Modified Porous $g\text{-}C_3N_4$ for Precious-Metal-Free Photocatalytic Hydrogen Evolution under Visible Light. *ACS Appl. Mater. Interfaces* **2019,** *11,* 5651–5660.

[14] Wang, X.; Kazuhiko, M.; Arne, T.; Kazuhiro, T.; Gang, X.; M., C. J.; Kazunari, D.; Markus, A. A Metal-Free Polymeric Photocatalyst for Hydrogen Production from Water under Visible Light. *Nat. Mater.* **2009**, *8*, 76–80.

[15] Huang, Z.; Song, J.; Pan, L.; Wang, Z. Carbon Nitride with Simultaneous Porous Network and O-Doping for Ef Fi Cient Solar-Energy-Driven Hydrogen Evolution. *Nano Energy* **2015**, *12*, 646–656.

[16] Li, X.; Zhao, S.; Duan, X.; Zhang, H.; Yang, S. ze; Zhang, P.; Jiang, S. P.; Liu, S.; Sun, H.; Wang, S. Coupling Hydrothermal and Photothermal Single-Atom Catalysis toward Excellent Water Splitting to Hydrogen. *Appl. Catal. B Environ.* **2021**, *283*, 119660.

[17] Li, X.; Zhang, H.; Liu, Y.; Duan, X.; Xu, X.; Liu, S.; Sun, H.; Wang, S. Synergy of NiO Quantum Dots and Temperature on Enhanced Photocatalytic and Thermophoto Hydrogen Evolution. *Chem. Eng. J.* **2020**, *390*, 124634.

[18] Zhang, J.; Li, Y.; Zhao, X.; Zhang, H.; Wang, L.; Chen, H.; Wang, S.; Xu, X.; Shi, L.; Zhang, L. C.; Veder, J. P.; Zhao, S.; Nealon, G.; Wu, M.; Wang, S.; Sun, H. A Hydrogen-Initiated Chemical Epitaxial Growth Strategy for In-Plane Heterostructured Photocatalyst. *ACS Nano* **2020**, *14* (12), 17505–17514.

[19] Yang, S.; Gong, Y.; Zhang, J.; Zhan, L.; Ma, L.; Fang, Z.; Vajtai, R.; Wang, X.; Ajayan, P. M. Exfoliated Graphitic Carbon Nitride Nanosheets as Efficient Catalysts for Hydrogen Evolution under Visible Light. *Adv. Mater.* **2013**, *25* (17), 2452–2456.

[20] Wu, J.; Li, N.; Zhang, X. H.; Fang, H. Bin; Zheng, Y. Z.; Tao, X. Heteroatoms Binary-Doped Hierarchical Porous $g\text{-}C_3N_4$ Nanobelts for Remarkably Enhanced Visible-Light-Driven Hydrogen Evolution. *Appl. Catal. B Environ.* **2018**, *226*, 61–70.

[21] Zhang, L.; Ding, N.; Lou, L.; Iwasaki, K.; Wu, H.; Luo, Y.; Li, D.; Nakata, K.; Fujishima, A.; Meng, Q. Localized Surface Plasmon Resonance Enhanced Photocatalytic Hydrogen Evolution via $Pt@Au\ NRs/C_3N_4$ Nanotubes under Visible-Light Irradiation. *Adv. Funct. Mater.* **2019**, *29* (3), 1–10.

[22] Fang, L. J.; Wang, X. L.; Zhao, J. J.; Li, Y. H.; Wang, Y. L.; Du, X. L.; He, Z. F.; Zeng, H. D.; Yang, H. G. One-Step Fabrication of Porous Oxygen-Doped $g\text{-}C_3N_4$ with Feeble Nitrogen Vacancies for Enhanced Photocatalytic Performance. *Chem. Commun.* **2016**, *52* (100), 14408–14411.

[23] Cheng, C.; Zong, S.; Shi, J.; Xue, F.; Zhang, Y.; Guan, X.; Zheng, B.; Deng, J.; Guo, L. Facile Preparation of Nanosized MoP as Cocatalyst Coupled with $G\text{-}C_3N_4$ by Surface Bonding State for Enhanced Photocatalytic Hydrogen Production. *Appl. Catal. B Environ.* **2020**, *265*, 118620.

[24] Zhu, Y.; Xu, Y.; Hou, Y.; Ding, Z.; Wang, X. Cobalt Sulfide Modified Graphitic Carbon Nitride Semiconductor for Solar Hydrogen Production. *Int. J. Hydrogen Energy* **2014**, *39* (23), 11873–11879.

[25] Ran, J.; Guo, W.; Wang, H.; Zhu, B.; Yu, J.; Qiao, S. Z. Metal-Free 2D/2D Phosphorene/$g\text{-}C_3N_4$ Van Der Waals Heterojunction for Highly Enhanced Visible-Light Photocatalytic H_2 Production. *Adv. Mater.* **2018**, *30* (25), 2–7.

[26] Li, H.; Tian, H.; Wang, X.; Pi, M.; Wei, S.; Zhu, H.; Zhang, D.; Chen, S. Self-Coupled $g\text{-}C_3N_4$ van Der Waals Heterojunctions for Enhanced Photocatalytic Hydrogen Production. *ACS Appl. Energy Mater.* **2019**, *2* (7), 4692–4699.

[27] Kresse, G.; Furthmüller, J.; Li, Y. J.; Chen, Y. J.; Walmsley, J. C.; Mathinsen, R. H.; Dumoulin, S.; Roven, H. J.; Yip, S.; Supervisor, T.; Chen, S. Modeling Microstructural E Ff Ects on Deformation Resistance and Thermal Conductivity. *Phys. Rev. B* **2000**, *62* (7), 11169–11186.

[28] Kresse, G.; Furthmüller, J. Efficiency of Ab-Initio Total Energy Calculations for Metals and Semiconductors Using a Plane-Wave Basis Set. *Comput. Mater. Sci.* **1996**, *6* (1), 15–50.

[29] Perdew, J. P.; Burke, K.; Ernzerhof, M. Generalized Gradient Approximation Made Simple. *Phys. Rev. Lett.* **1996**, *77* (18), 3865–3868.

[30] Grimme, S.; Antony, J.; Ehrlich, S.; Krieg, H. A Consistent and Accurate Ab Initio Parametrization of Density Functional Dispersion Correction (DFT-D) for the 94 Elements H-Pu. *J. Chem. Phys.* **2010**, *132* (15), 154104.

[31] Momma, K.; Izumi, F. VESTA 3 for Three-Dimensional Visualization of Crystal, Volumetric and Morphology Data. *J. Appl. Crystallogr.* **2011**, *44* (6), 1272–1276.

[32] Liu, J.; Jia, Q.; Long, J.; Wang, X.; Gao, Z.; Gu, Q. Amorphous NiO as Co-Catalyst for Enhanced Visible-Light-Driven Hydrogen Generation over $g\text{-}C_3N_4$ Photocatalyst. *Appl. Catal. B Environ.* **2018**, *222*, 35–43.

[33] Suryawanshi, A.; Dhanasekaran, P.; Mhamane, D.; Kelkar, S.; Patil, S.; Gupta, N.; Ogale, S. Doubling of Photocatalytic H_2 Evolution from $G\text{-}C_3N_4$ via Its Nanocomposite Formation with Multiwall Carbon Nanotubes: Electronic and Morphological Effects. *Int. J. Hydrogen Energy* **2012**, *37* (12), 9584–9589.

[34] Fang, Z.; Hong, Y.; Li, D.; Luo, B.; Mao, B.; Shi, W. One-Step Nickel Foam Assisted Synthesis of Holey G - Carbon Nitride Nanosheets for Efficient Visible-Light Photocatalytic H_2 Evolution. **2018,** *10*, 20521–20529.

[35] Liu, J.; Zhang, T.; Wang, Z.; Dawson, G.; Chen, W. Simple Pyrolysis of Urea into Graphitic Carbon Nitride with Recyclable Adsorption and Photocatalytic Activity. *J. Mater. Chem.* **2011**, *21* (38), 14398–14401.

[36] Zhang, M.; Bai, X.; Liu, D.; Wang, J.; Zhu, Y. Enhanced Catalytic Activity of Potassium-Doped Graphitic Carbon Nitride Induced by Lower Valence Position. *Appl. Catal. B Environ.* **2015**, *164*, 77–81.

[37] Wang, Y.; Zhao, S.; Zhang, Y.; Fang, J.; Zhou, Y.; Yuan, S.; Zhang, C.; Chen, W. One-Pot Synthesis of K-Doped $g\text{-}C_3N_4$ Nanosheets with Enhanced Photocatalytic Hydrogen Production under Visible-Light Irradiation. *Appl. Surf. Sci.* **2018**, *440*, 258–265.

[38] Babu, P.; Mohanty, S.; Naik, B.; Parida, K. Synergistic Effects of Boron and Sulfur Co-Doping into Graphitic Carbon Nitride Framework for Enhanced Photocatalytic Activity in Visible Light Driven Hydrogen Generation. *ACS Appl. Energy Mater.* **2018**, *1* (11), 5936–5947.

[39] Chen, P.; Xing, P.; Chen, Z.; Lin, H.; He, Y. Rapid and Energy-Efficient Preparation of Boron Doped $g\text{-}C_3N_4$ with Excellent Performance in Photocatalytic H_2-Evolution. *Int. J. Hydrogen Energy* **2018**, *43* (43), 19984–19989.

[40] Guo, Y.; Liu, Q.; Li, Z.; Zhang, Z.; Fang, X. Enhanced Photocatalytic Hydrogen Evolution Performance of Mesoporous Graphitic Carbon Nitride Co-Doped with Potassium and Iodine. *Appl. Catal. B Environ.* **2018**, *221*, 362–370.

[41] Wu, M.; Yan, J. M.; Zhang, X. W.; Zhao, M.; Jiang, Q. Ag_2O Modified $G\text{-}C_3N_4$ for Highly Efficient Photocatalytic Hydrogen Generation under Visible Light Irradiation. *J. Mater. Chem. A* **2015**, *3* (30), 15710–15714.

[42] Yang, L.; Liu, J.; Yang, L.; Zhang, M.; Zhu, H.; Wang, F.; Yin, J. Co_3O_4 Imbedded $G\text{-}C_3N_4$ Heterojunction Photocatalysts for Visible-Light-Driven Hydrogen Evolution. *Renew. Energy* **2020**, *145*, 691–698.

[43] Xu, H.; Yi, J.; She, X.; Liu, Q.; Song, L.; Chen, S.; Yang, Y.; Song, Y.;

Vajtai, R.; Lou, J.; Li, H.; Yuan, S.; Wu, J.; Ajayan, P. M. 2D Heterostructure Comprised of Metallic 1T-MoS_2/Monolayer O-g-C_3N_4 towards Efficient Photocatalytic Hydrogen Evolution. *Appl. Catal. B Environ.* **2018**, *220*, 379–385.

[44] Wang, Y.; Wang, X.; Antonietti, M. Polymeric Graphitic Carbon Nitride as a Heterogeneous Organocatalyst: From Photochemistry to Multipurpose Catalysis to Sustainable Chemistry. *Angew. Chemie - Int. Ed.* **2012**, *51* (1), 68–89.

[45] Schwinghammer, K.; Mesch, M. B.; Duppel, V.; Ziegler, C.; Senker, J.; Lotsch, B. V. Crystalline Carbon Nitride Nanosheets for Improved Visible-Light Hydrogen Evolution. *J. Am. Chem. Soc.* **2014**, *136* (5), 1730–1733.

[46] Wang, Y.; Zhang, Y.; Zhao, S.; Huang, Z.; Chen, W.; Zhou, Y.; Lv, X.; Yuan, S. Bio-Template Synthesis of Mo-Doped Polymer Carbon Nitride for Photocatalytic Hydrogen Evolution. *Appl. Catal. B Environ.* **2019**, *248*, 44–53.

[47] Liu, Y.; Zhang, H.; Ke, J.; Zhang, J.; Tian, W.; Xu, X.; Duan, X.; Sun, H.; O Tade, M.; Wang, S. 0D (MoS_2)/2D (g-C_3N_4) Heterojunctions in Z-Scheme for Enhanced Photocatalytic and Electrochemical Hydrogen Evolution. *Appl. Catal. B Environ.* **2018**, *228*, 64–74.

[48] Han, Q.; Zhao, F.; Hu, C.; Lv, L.; Zhang, Z.; Chen, N.; Qu, L. Facile Production of Ultrathin Graphitic Carbon Nitride Nanoplatelets for Efficient Visible-Light Water Splitting. *Nano Res*., **2015**, *8* (5), 1718–1728.

[49] Ma, L.; Fan, H.; Wang, J.; Zhao, Y.; Tian, H.; Dong, G. Water-Assisted Ions in Situ Intercalation for Porous Polymeric Graphitic Carbon Nitride Nanosheets with Superior Photocatalytic Hydrogen Evolution Performance. *Applied Catal. B, Environ.* **2016**, *190*, 93–102.

[50] Wang, K.; Li, Q.; Liu, B.; Cheng, B.; Ho, W.; Yu, J. Sulfur-Doped g-C_3N_4 with Enhanced Photocatalytic CO_2-Reduction Performance. *Appl. Catal. B Environ.* **2015**, *176–177*, 44–52.

Electronic Supplementary Material

van der Waals type II carbon nitride homojunctions for visible light photocatalytic hydrogen evolution

Xiaojie Li[1,2], Panpan Zhang[1], Huayang Zhang[1], Wenjie Tian[1], Yangyang Yang[1], Kunsheng Hu[1], Dechao Chen[3], Qin Li[3], Xiaoguang Duan[1], Hongqi Sun[4] (✉), Shaobin Wang[1] (✉)

[1] *School of Chemical Engineering and Advanced Materials, The University of Adelaide, Adelaide, SA 5005, Australia*

[2] *Department of Chemical Engineering, Curtin University, GPO Box U1987, Perth, WA 6845, Australia*

[3] *Queensland Micro- and Nanotechnology Centre, School of Engineering and Built Environment, Griffith University, Nathan, QLD 4111, Australia*

[4] *School of Engineering, Edith Cowan University, Joondalup, WA 6027, Australia*

Supporting information to DOI 10.1007/s12274-****-****-* (automatically inserted by the publisher)

Table S1. The sum of valence electrons in calculation results.

Materials	Carbon/Atomic number	Pyridinic N/Atomic number	Graphitic N connected with three tri-s-triazine moieties (GNTT)/Atomic number
CN (Fig. S3)	59.0884 (C1-C24)	147.6636 (N25-N30, N33-N38, N41-N46, N49-N54)	24.4272 (N31, N39, N47, N55)
BCN (B substituting C) (BCN-C) (Fig. S4)	55.862 (C1-C23)	148.5794 (N1-6, N9-N14, N17-N22, N25-N30)	24.6661 (N7, N15, N23, N31)
BCN (B substituting the N connected with three tri-s-triazine moieties) (BCN-N) (Fig. S5)	62.0933 (C1-C24)	147.6599 (N1-6, N9-N14, N17-N22, N25-N30)	18.1465 (N7, N15, N23)
KCN (Fig. S6)	59.3578 (C1-C24)	148.378 (N1-6, N9-N14, N17-N22, N25-N30)	24.7489 (N7, N15, N23, N31)

Table S2. Comparison of the specific surface area (m^2/g) of samples.

Bulk vs. Nanosheets		Pure vs. Doping		vdW type II junctions		Mixture	
CN:	99.1	CN:	99.1	CN-BCN-S	90.9	CNS-BCNS:	116
CNS:	144	BCN:	65.8	CN-KCN-S	87.1	CNS-KCNS:	101
BCN:	65.8	KCN:	61.7	BCN-KCN-S	94.2	BCNS-KCNS:	99.4
BCNS:	104	CNS:	144	CN-BCN-KCN-S	84.8	CNS-BCNS-KCNS:	112
KCN:	61.7	BCNS:	104				
KCNS:	103	KCNS:	103				

Table S3. A comparison of the photocatalytic H_2-production activities for doped g-C_3N_4.

Photocatalyst	Optical source	Sacrificial agent	H_2 evolution ($\mu mol \cdot h^{-1} \cdot g^{-1}$)	Enhanced degree	Ref.
3 wt% Pt/Cl doped g-C_3N_4	(300 W, > 400 nm) Xe lamp	10% TEOA	833	1.54	[1]
3 wt% Pt/Br doped g-C_3N_4	(300 W, >420 nm) Xe lamp	10% TEOA	960	2.4	[2]
3 wt% Pt/I doped g-C_3N_4 NS	(300 W, >420 nm) Xe lamp	10% TEOA	890	2.3	[3]
1.2 wt% Pt/O doped g-C_3N_4	(300 W, >420 nm) Xe lamp	10% TEOA	375	2.5	[4]
6 wt% Pt/S doped g-C_3N_4	(300 W, >420 nm) Xe lamp	10% TEOA	333	8	[5]
3 wt% Pt/N doped g-C_3N_4	(300 W, > 400 nm) Xe lamp	10% TEOA	554	5.6	[6]
3 wt% Pt/P doped g-C_3N_4	(300 W, >420 nm) Xe lamp	10% TEOA	506	2.9	[7]
3 wt% Pt/C-doped g-C_3N_4	(> 420 nm) Xe lamp	10% TEOA	1889	4.7	[8]
3 wt% Pt/Co doped g-C_3N_4	(300 W, >420 nm) Xe lamp	10% TEOA	560	3	[9]
1.5 wt% Pt/Mo-Co-mpg-C_3N_4	(300 W, > 400 nm) Xe lamp	10% TEOA	694.5	8.6	[10]
3 wt% Pt/CN-KCN-S	(300 W, >420 nm) Xe lamp	10% TEOA	1243	8.9	This study

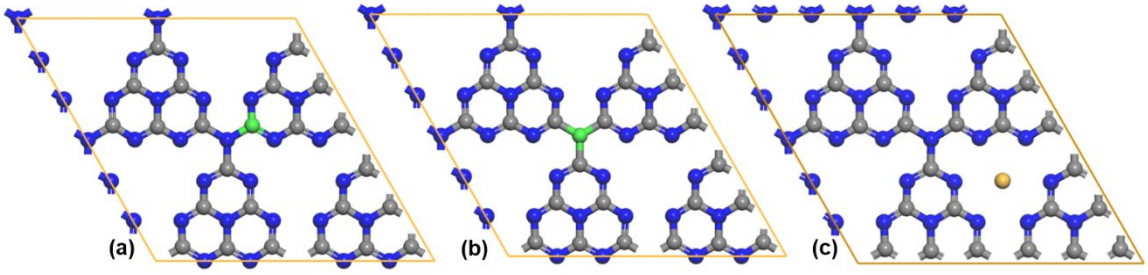

Scheme S1. The chemical structures of (a) B doped g-C_3N_4 with B substituting C, (b) B doped g-C_3N_4 with B substituting the N atoms connected with three tri-s-triazine moieties, and (c) K doped g-C_3N_4. Blue for nitrogen atoms, grey for carbon atoms, green for boron atoms and yellow for potassium atoms.

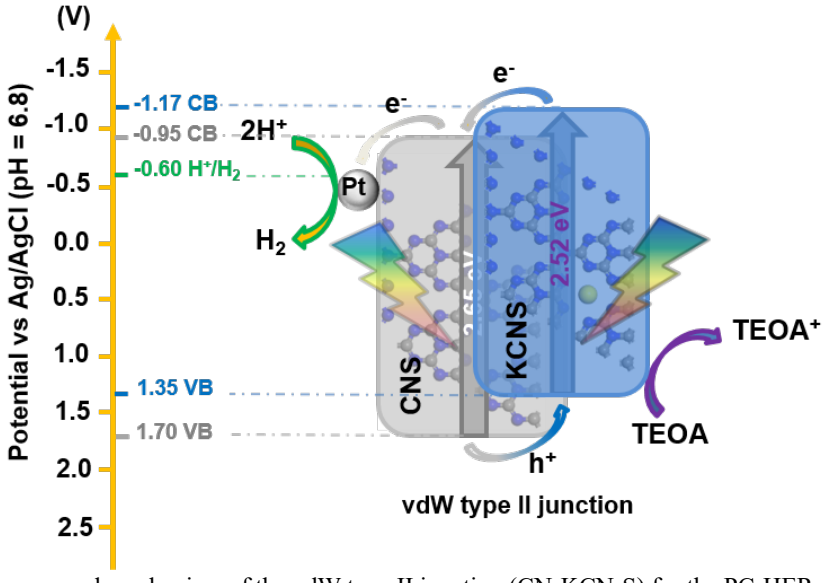

Scheme S2. The traditionally proposed mechanism of the vdW type II junction (CN-KCN-S) for the PC-HER process. Under visible light (> 420 nm), photo-excited electrons are obtained in the CB positions of both CNS and KCNS. The photoelectrons from KCNS are then transferred to the CB of CNS via their vast "face to face" vdW contact and then go to the platinum cocatalyst together with the photoelectrons from the CNS. Afterwards, the hydrogen ions from water react with the electrons on platinum nanoparticles, so that hydrogen gas molecules are generated. Simultaneously, the photo-motivated holes from the VB of CNS firstly fall to the CB of KCNS, and are then, along with the photo-holes originating from KCNS, consumed by the sacrificial agent of TEOA. Herein, all the factors, including the cocatalyst, sacrificial agent, charge transfer in the type II structure, shortened bandgap of KCNS than that of CNS, large specific surface area of the nanosheets, and vast "face to face" vdW contact, are synergistically contributing to the PC-HER process.

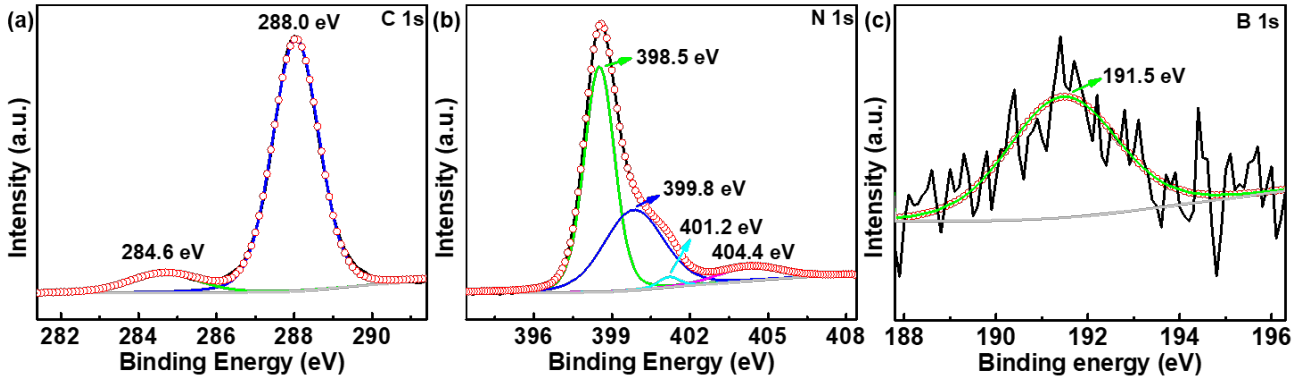

Fig. S1. XPS spectra of BCN. (a) C 1s, (b) N 1s, and (c) B 1s.

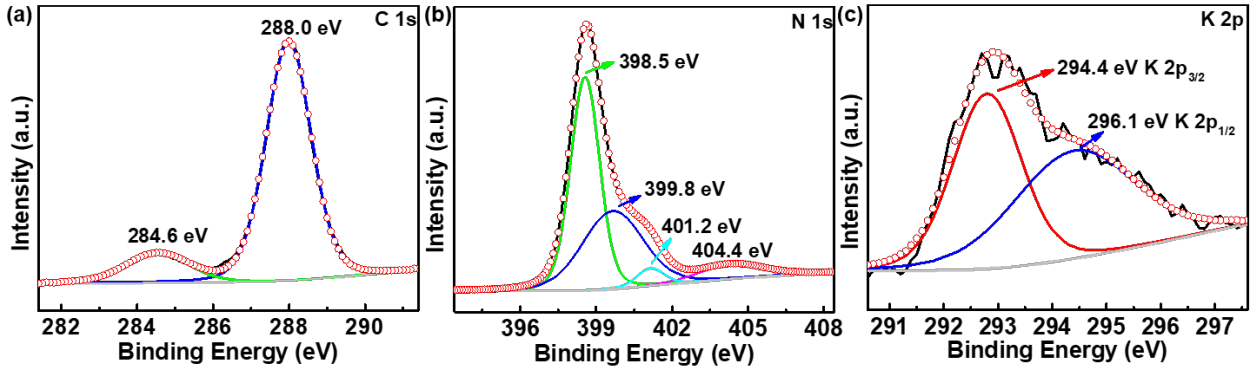

Fig. S2. XPS spectra of KCN. (a) C 1s, (b) N 1s, and (c) K 2p.

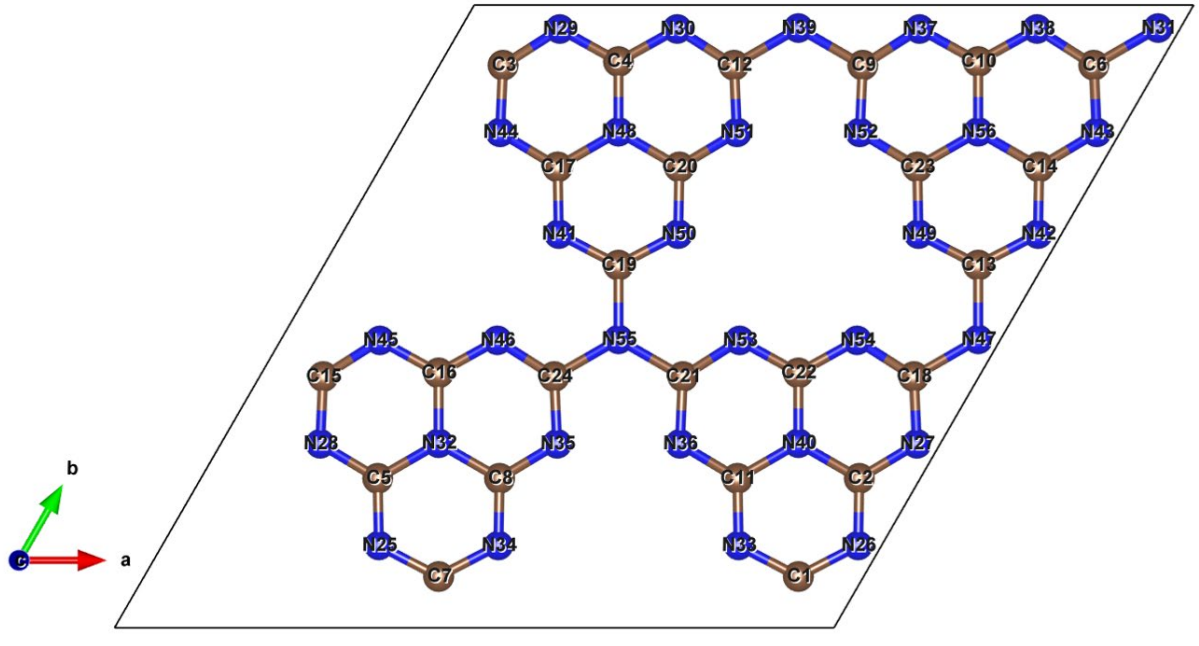

Fig. S3. The atomic number of CN for Table S1.

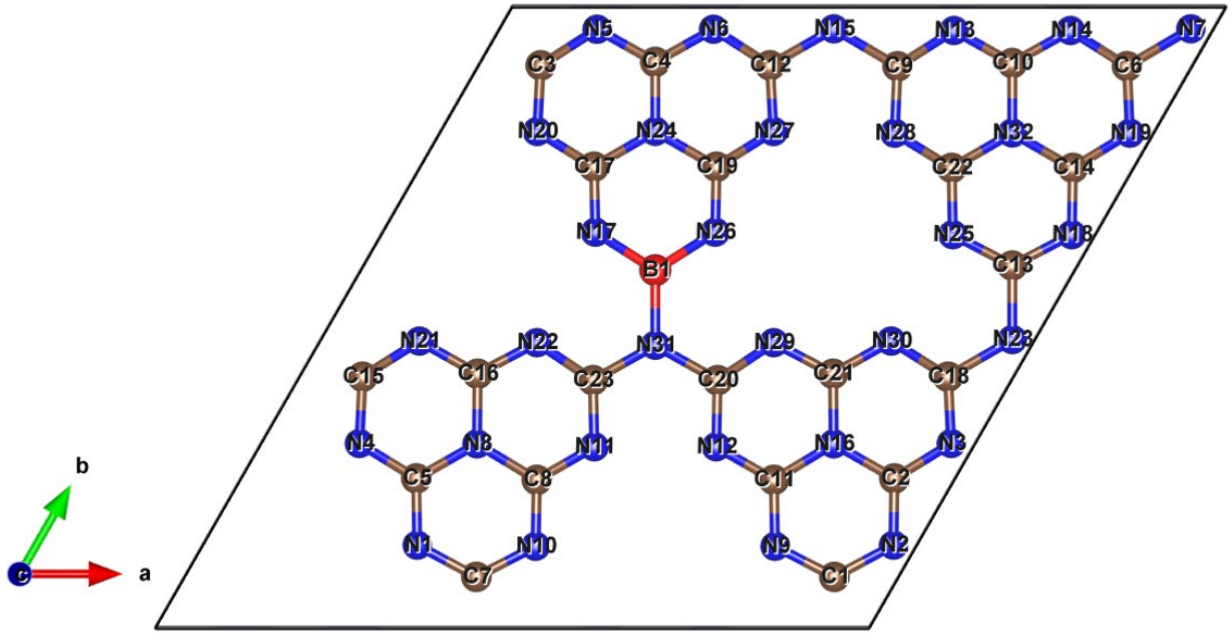

Fig. S4. The atomic number of BCN (B substituting C) (BCN-C) for Table S1.

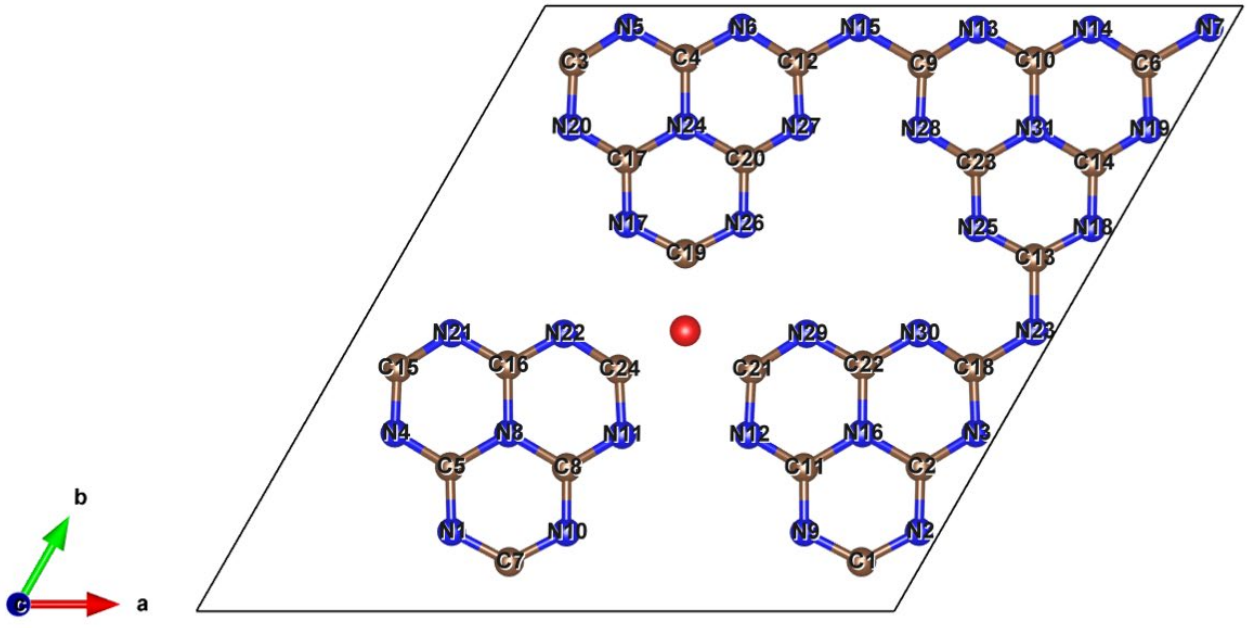

Fig. S5. The atomic number of BCN (substituting the N connected with three tri-s-triazine moieties) (BCN-N) for Table S1. Red for B atom.

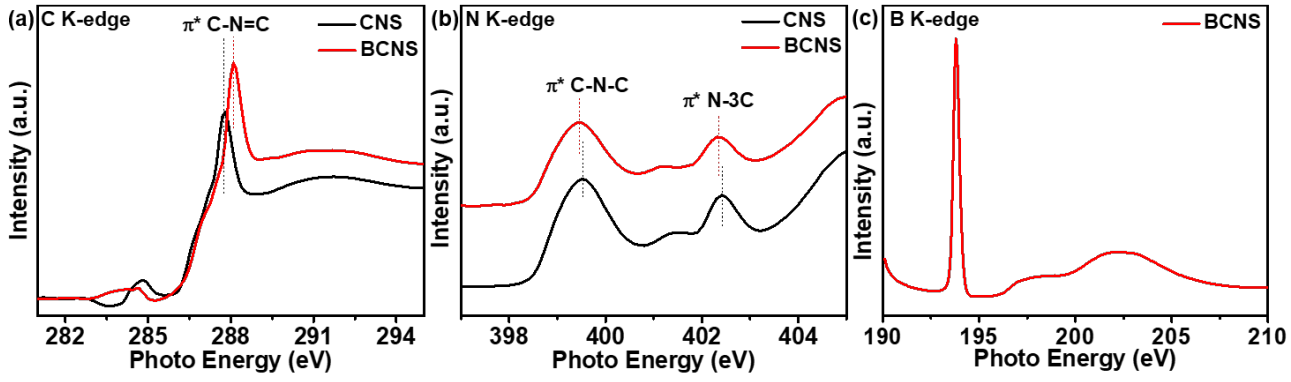

Fig. S6. The NEXAFS profiles of BCNS. (a) C K-edge, (b) N K-edge, and (c) B K-edge.

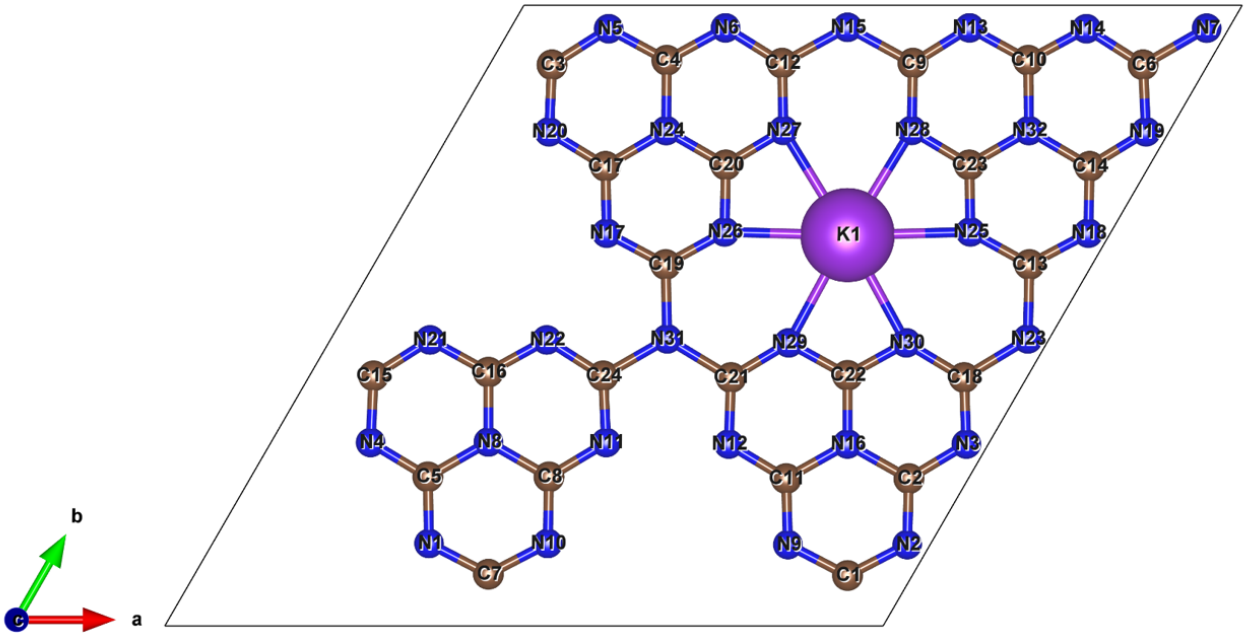

Fig. S7. The atomic number of KCN for Table S1.

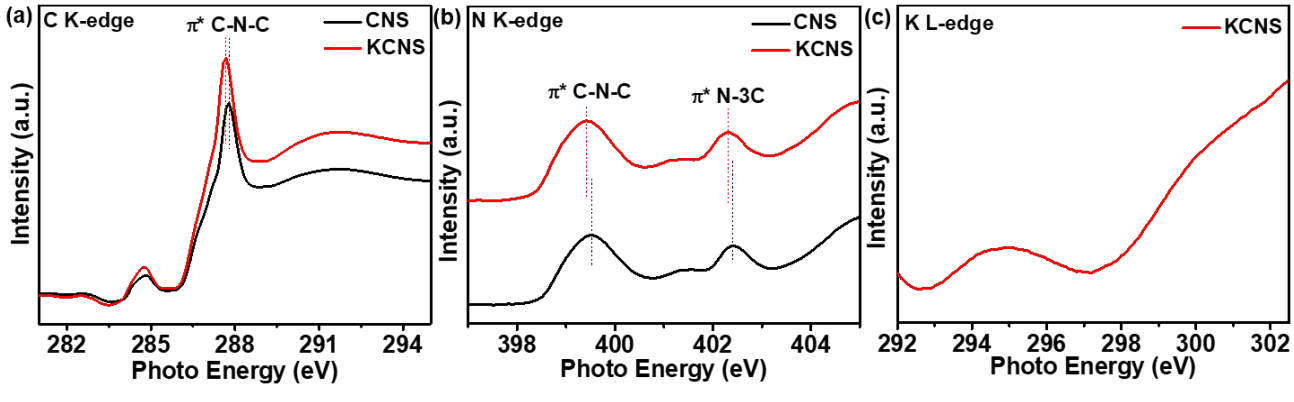

Fig. S8. The NEXAFS spectra of KCNS. (a) C K-edge, (b) N K-edge, and (c) K L-edge.

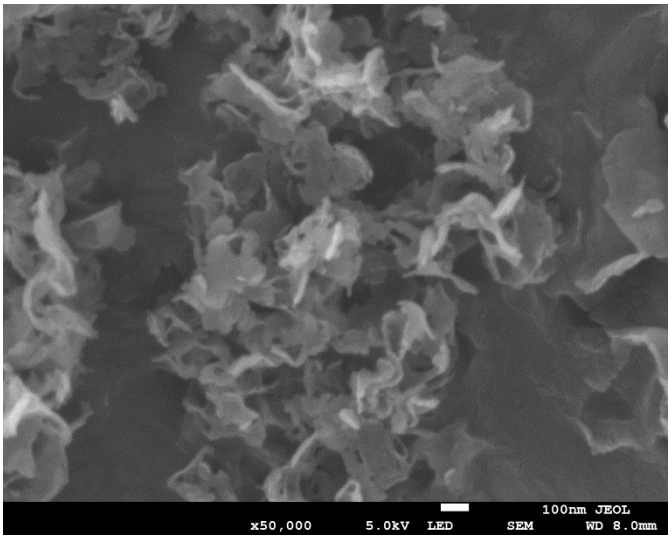

Fig. S9. The SEM image of CN-KCN-S.

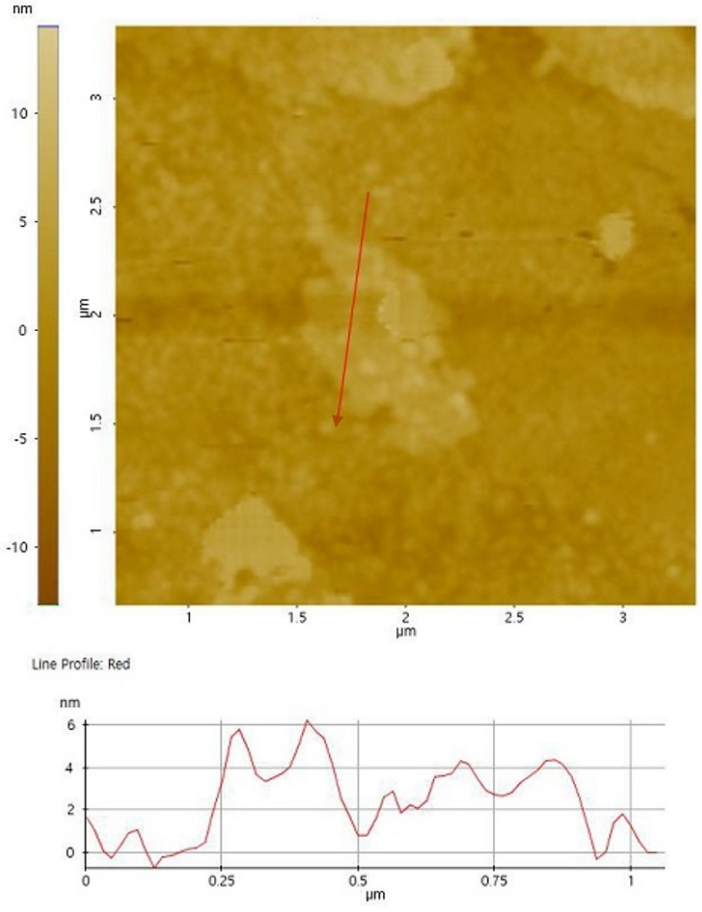

Fig. S10. The AFM image of CN-KCN-S.

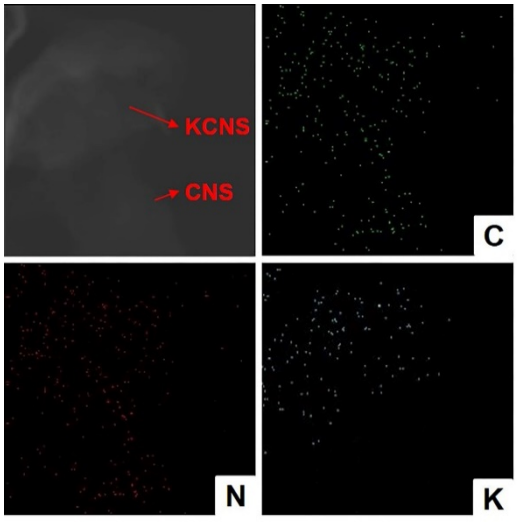

Fig. S11. The EDS elemental mapping image of CN-KCN-S.

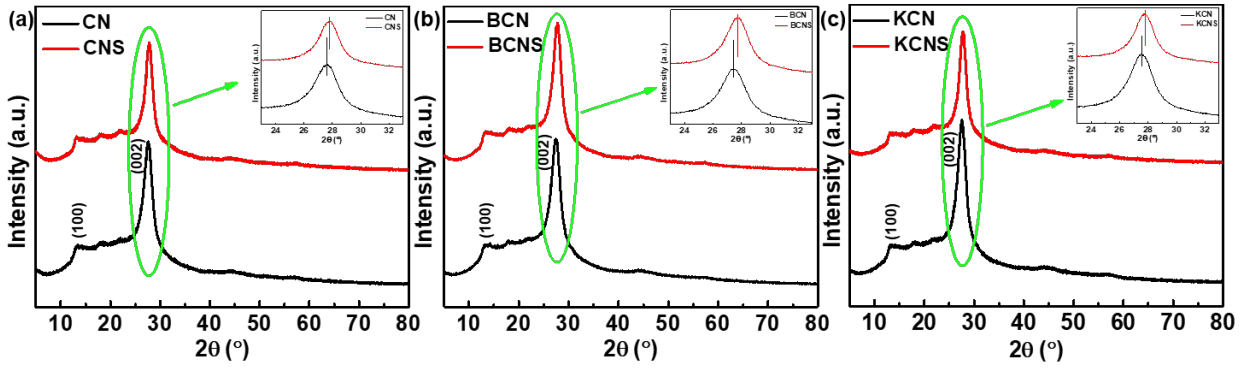

Fig. S12. XRD patterns of bulk materials and nanosheets. (a) CN vs. CNS, (b) BCN vs. BCNS, and (c) KCN vs. KCNS.

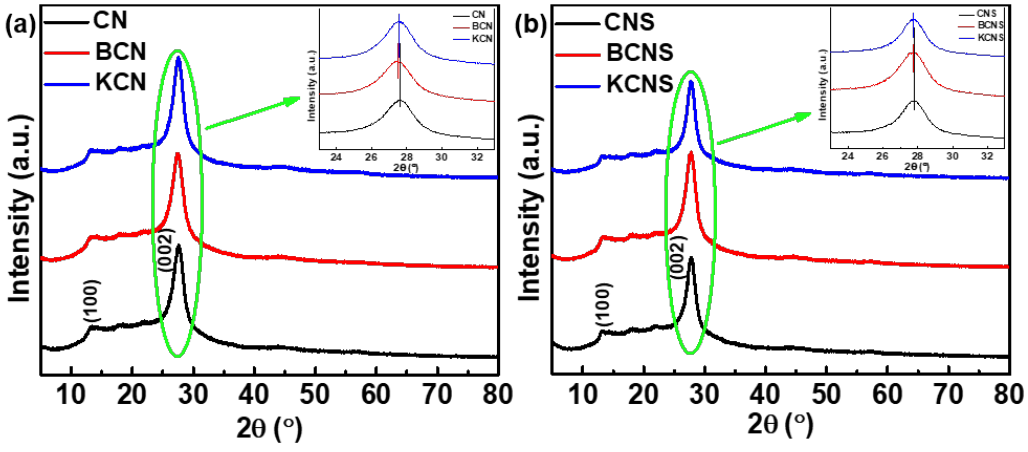

Fig. S13. XRD patterns of doped g-C_3N_4 and pristine g-C3N4. (a) CN vs. BCN vs. KCN, and (b) CNS vs. BCNS vs. KCNS.

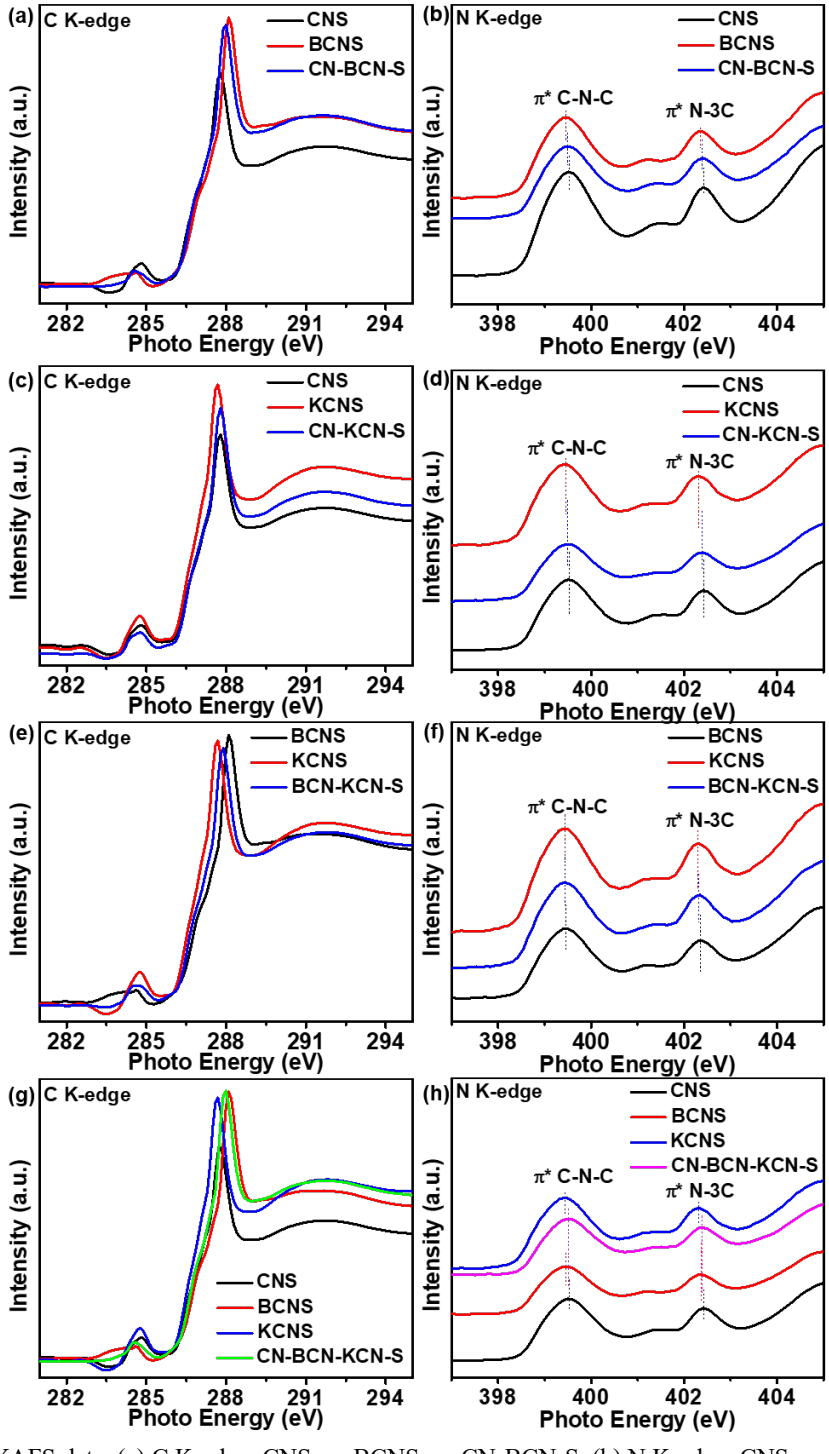

Fig. S14. Comparison of NEXAFS data. (a) C K-edge, CNS vs. BCNS vs. CN-BCN-S. (b) N K-edge, CNS vs. BCNS vs. CN-BCN-S. (c) C K-edge, CNS vs. KCNS vs. CN-KCN-S. (d) N K-edge, CNS vs. KCNS vs. CN-KCN-S. (e) C K-edge, BCNS vs. KCNS vs. BCN-KCN-S. (f) N K-edge, BCNS vs. KCNS vs. BCN-KCN-S. (g) C K-edge, CNS vs. BCNS vs. KCNS vs. CN-BCN-KCN-S. (h) N K-edge, CNS vs. BCNS vs. KCNS vs. CN-BCN-KCN-S.

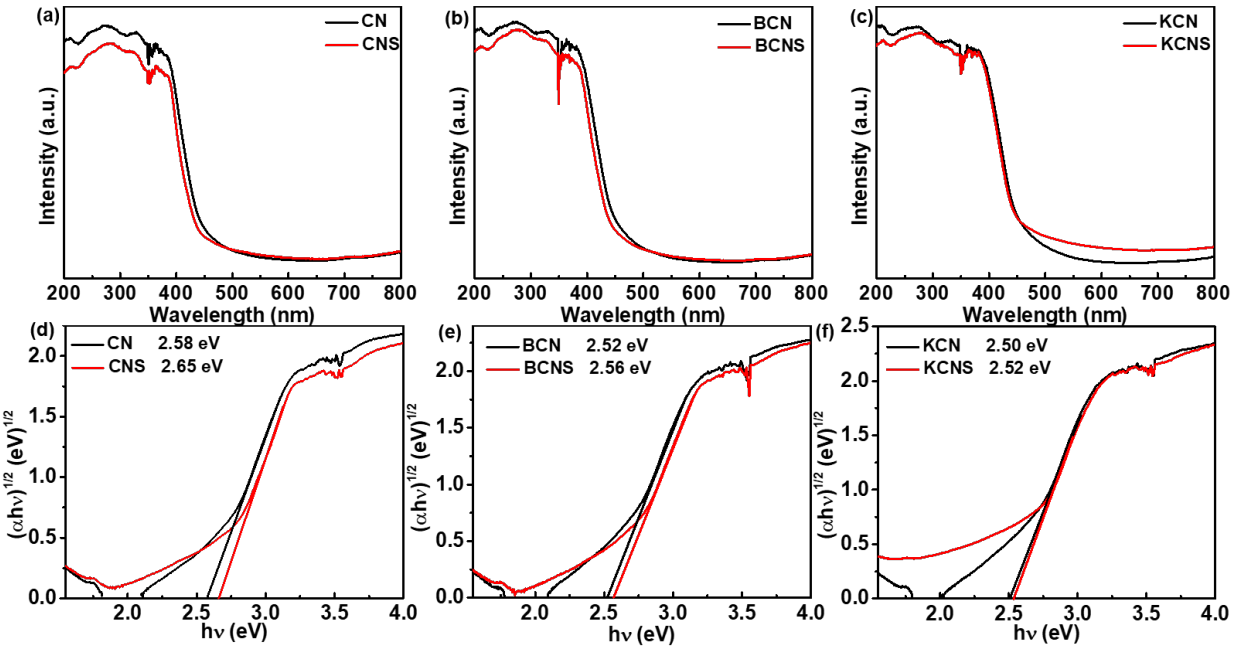

Fig. S15. UV-vis diffuse reflectance spectra of bulk materials and nanosheets. (a) CN vs. CNS, (b) BCN vs. BCNS, (c) KCN vs. KCNS. The plots of (αhν)1/2 vs. bandgap energy (hν) of bulk materials and nanosheets. (d) CN vs. CNS, (e) BCN vs. BCNS, (f) KCN vs. KCNS.

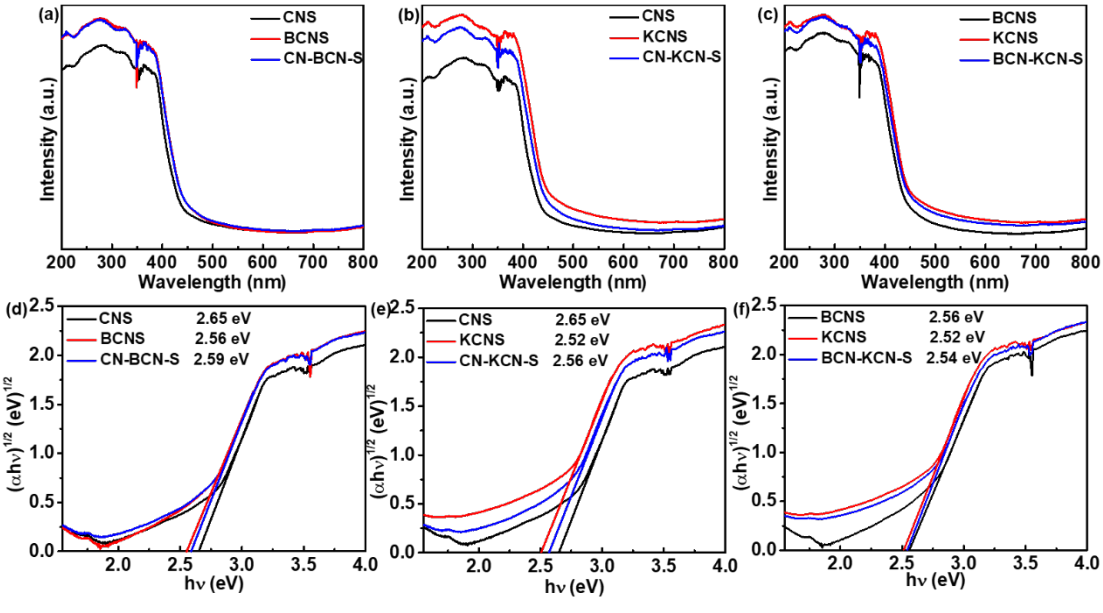

Fig. S16. UV-vis diffuse reflectance spectra of the vdW type II and corresponding nanosheet materials of (a) CNS vs. BCNS vs. CN-BCN-S, (b) CNS vs. KCNS vs. CN-KCN-S, and (c) BCNS vs. KCNS vs. BCN-KCN-S; and their matching plots of $(\alpha h\nu)^{1/2}$ vs. bandgap energy (hν) of (d) CNS vs. BCNS vs. CN-BCN-S, (e) CNS vs. KCNS vs. CN-KCN-S, and (f) BCNS vs. KCNS vs. BCN-KCN-S.

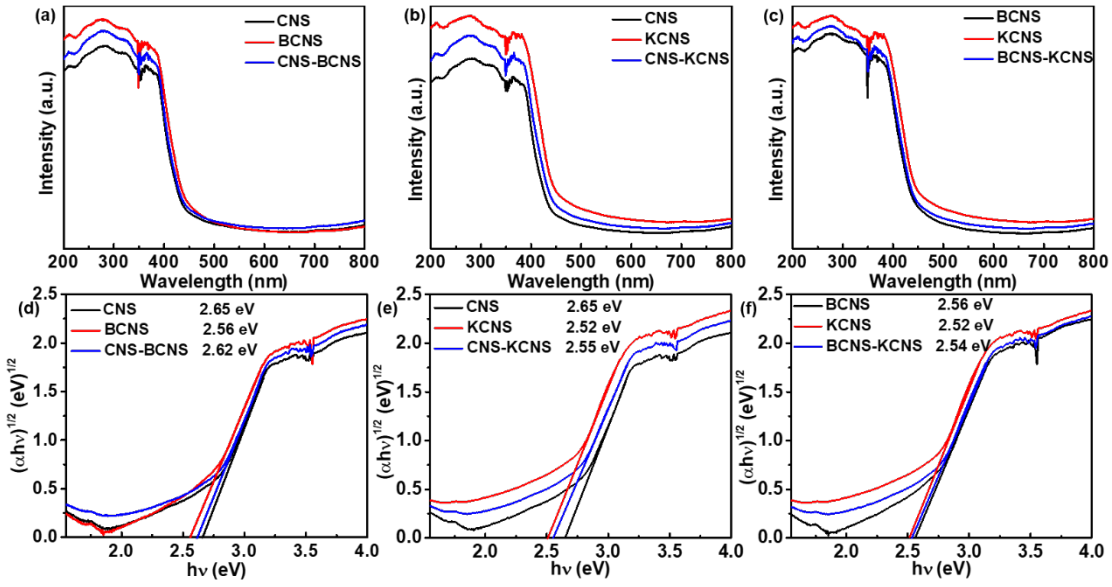

Fig. S17. UV-vis diffuse reflectance spectra of the mixture and corresponding nanosheet materials of (a) CNS vs. BCNS vs. CNS-BCNS, (b) CNS vs. KCNS vs. CNS-KCNS, and (c) BCNS vs. KCNS vs. BCNS-KCNS; and their matching plots of $(\alpha h\nu)^{1/2}$ vs. bandgap energy ($h\nu$) of (d) CNS vs. BCNS vs. CNS-BCNS, (e) CNS vs. KCNS vs. CNS-KCNS, and (f) BCNS vs. KCNS vs. BCNS-KCNS.

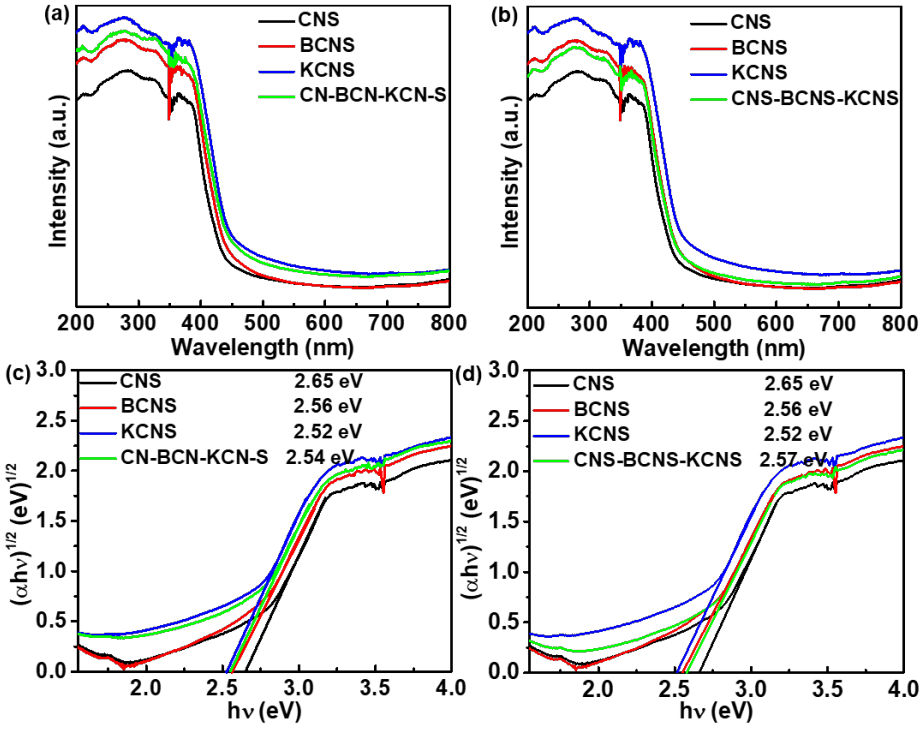

Fig. S18. UV-vis diffuse reflectance spectra of the vdW binary type II, the ternary mixture, and corresponding nanosheet materials of (a) CNS vs. BCNS vs. KCNS vs. CN-BCN-KCN-S, and (b) CNS vs. BCNS vs. KCNS vs. CNS-BCNS-KCNS; and their matching plots of $(\alpha h\nu)^{1/2}$ vs. bandgap energy ($h\nu$) of (c) CNS vs. BCNS vs. KCNS vs. CN-BCN-KCN-S, and (d) CNS vs. BCNS vs. KCNS vs. CNS-BCNS-KCNS.

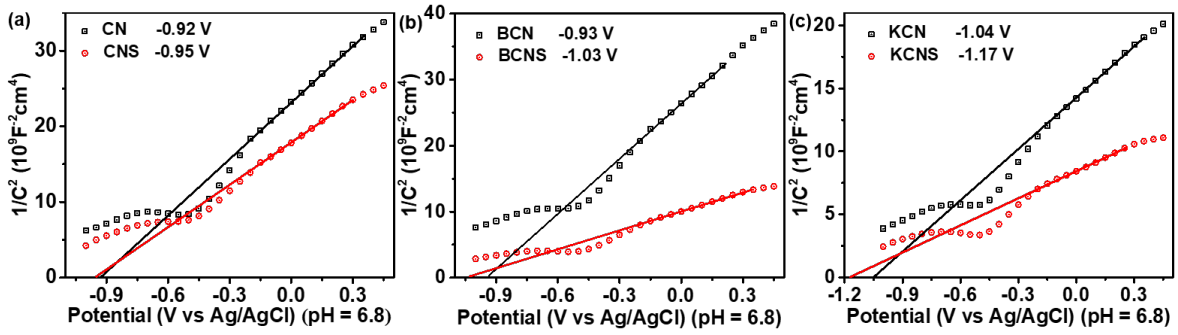

Fig. S19. The Mott-Schottky curves of bulk materials and corresponding nanosheets. (a) CN vs. CNS, (b) BCN vs. BCNS, (c) KCN vs. KCNS.

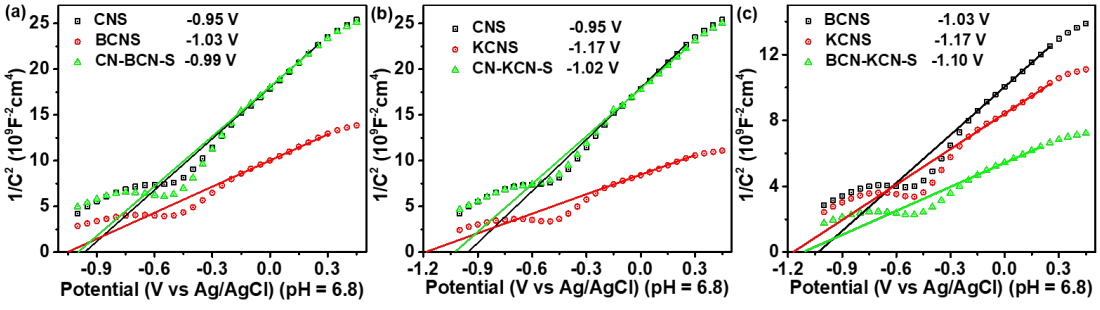

Fig. S20. The Mott-Schottky curves of the vdW type II and corresponding nanosheet materials (a) CNS vs. BCNS vs. CN-BCN-S, (b) CNS vs. KCNS vs. CN-KCN-S, and (c) BCNS vs. KCNS vs. BCN-KCN-S.

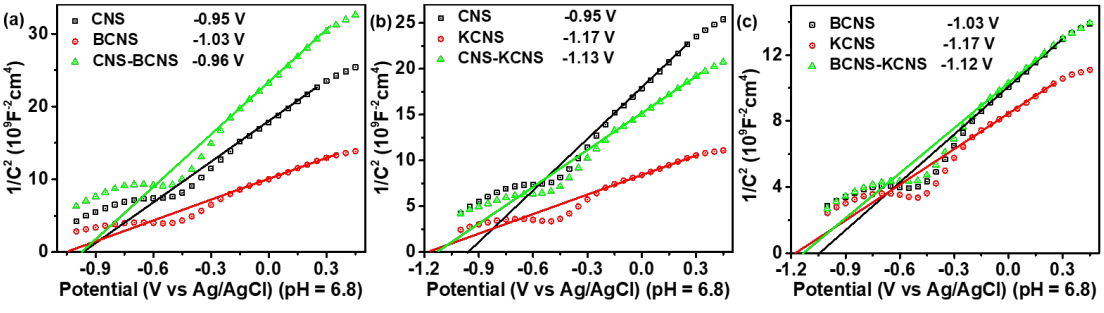

Fig. S21. The Mott-Schottky curves of the binary mixture and corresponding nanosheet materials (a) CNS vs. BCNS vs. CNS-BCNS, (b) CNS vs. KCNS vs. CNS-KCNS, and (c) BCNS vs. KCNS vs. BCNS-KCNS.

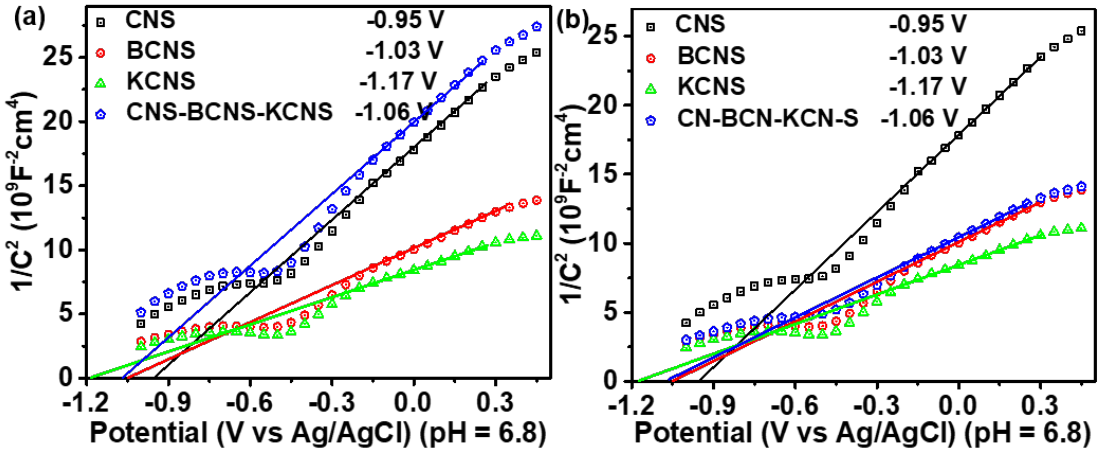

Fig. S22. The Mott-Schottky curves of the vdW binary type II, the ternary mixture, and corresponding nanosheet materials of (a) CNS vs. BCNS vs. KCNS vs. CN-BCN-KCN-S, and (b) CNS vs. BCNS vs. KCNS vs. CNS-BCNS-KCNS.

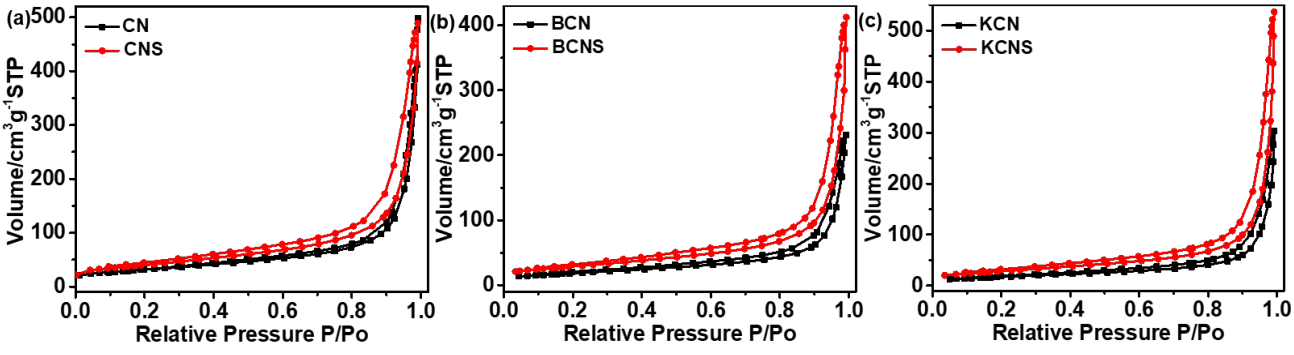

Fig. S23. N_2 adsorption-desorption isotherms of (a) CN vs. CNS, (b) BCN vs. BCNS, and (c) KCN vs. KCNS.

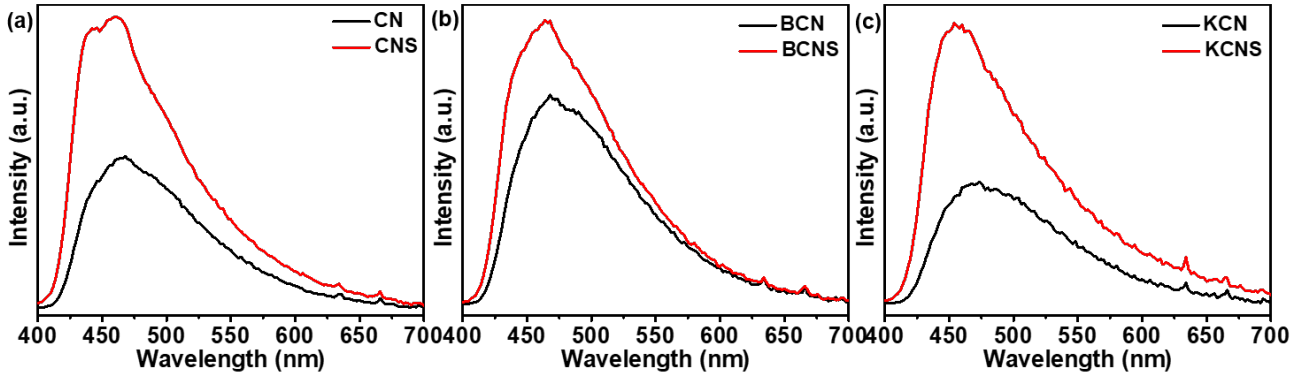

Fig. S24. The PL intensities of bulk materials and corresponding nanosheets. (a) CN vs. CNS, (b) BCN vs. BCNS, (c) KCN vs. KCNS.

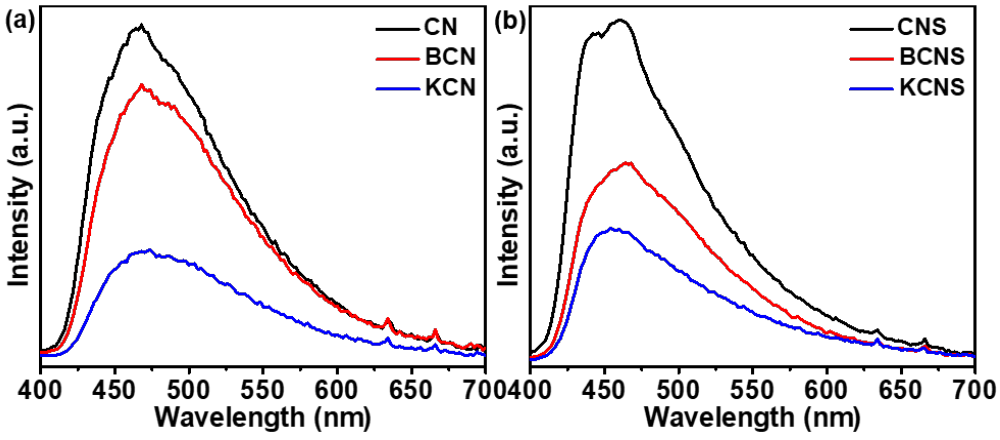

Fig. S25. PL intensities of heteroatom-doping and non-doping g-C_3N_4 based materials of (a) CN vs. BCN vs. KCN, and (b) CNS vs. BCNS vs. KCNS.

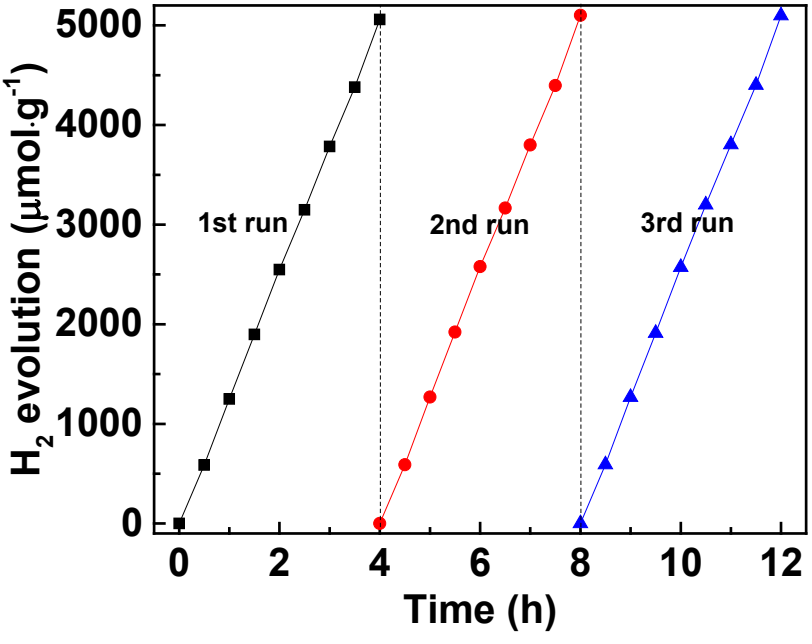

Fig. S26. The cycle runs for the photocatalytic H2 evolution on CN-KCN-S.

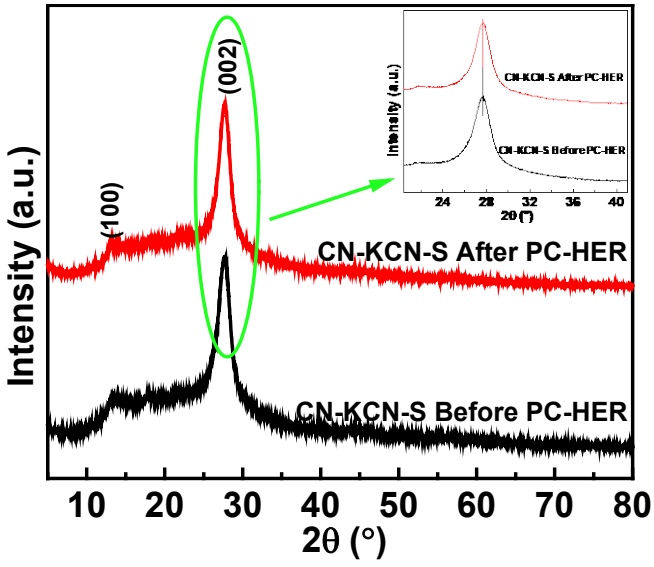

Fig. S27. XRD patterns of CN-KCN-S before and after PC-HER test.

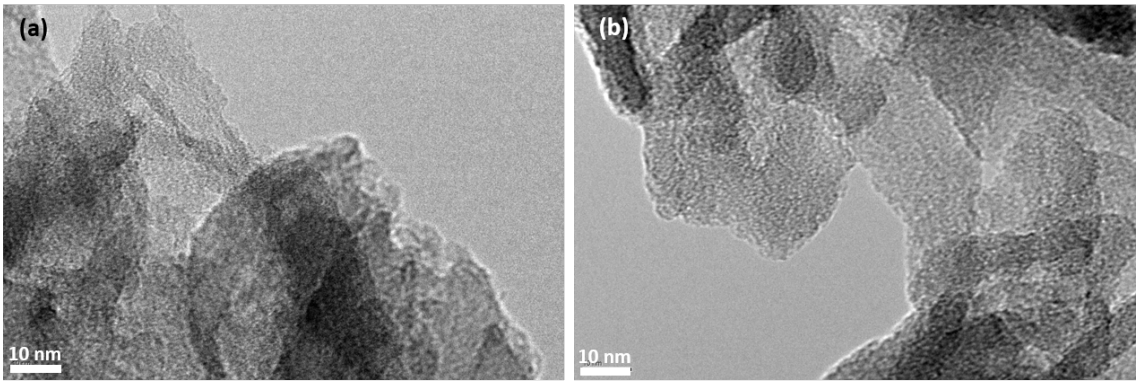

Fig. S28. TEM images of CN-KCN-S (a) before and (b) after PC-HER test.

References

[1] Shi, L.; Wang, F.; Sun, J. The Preparation of Spherical Mesoporous G-C_3N_4 with Highly Improved Photocatalytic Performance for H_2 Production and Rhodamine B Degradation. *Mater. Res. Bull.* **2019**, *113*, 115–121.

[2] Lan, Z. A.; Zhang, G.; Wang, X. A Facile Synthesis of Br-Modified g-C_3N_4 Semiconductors for Photoredox Water Splitting. *Appl. Catal. B Environ.* **2016**, *192*, 116–125.

[3] Han, Q.; Hu, C.; Zhao, F.; Zhang, Z.; Chen, N.; Qu, L. One-Step Preparation of Iodine-Doped Graphitic Carbon Nitride Nanosheets as Efficient Photocatalysts for Visible Light Water Splitting. *J. Mater. Chem. A* **2015**, *3* (8), 4612–4619.

[4] Li, J.; Shen, B.; Hong, Z.; Lin, B.; Gao, B.; Chen, Y. A Facile Approach to Synthesize Novel Oxygen-Doped g-C_3N_4 with Superior Visible-Light Photoreactivity. *Chem. Commun.* **2012**, *48* (98), 12017–12019.

[5] Liu, G.; Niu, P.; Sun, C.; Smith, S. C.; Chen, Z.; Lu, G. Q.; Cheng, H. M. Unique Electronic Structure Induced High Photoreactivity of Sulfur-Doped Graphitic C_3N_4. *J. Am. Chem. Soc.* **2010**, *132* (33), 11642–11648.

[6] Fang, J.; Fan, H.; Li, M.; Long, C. Nitrogen Self-Doped Graphitic Carbon Nitride as Efficient Visible Light Photocatalyst for Hydrogen Evolution. *J. Mater. Chem. A* **2015**, *3* (26), 13819–13826.

[7] Zhou, Y.; Zhang, L.; Liu, J.; Fan, X.; Wang, B.; Wang, M.; Ren, W.; Wang, J.; Li, M.; Shi, J. Brand New P-Doped g-C_3N_4: Enhanced Photocatalytic Activity for H_2 Evolution and Rhodamine B Degradation under Visible Light. *J. Mater. Chem. A* **2015**, *3* (7), 3862–3867.

[8] Zhang, L.; Jin, Z.; Huang, S.; Huang, X.; Xu, B.; Hu, L.; Cui, H.; Ruan, S.; Zeng, Y. J. Bio-Inspired Carbon Doped Graphitic Carbon Nitride with Booming Photocatalytic Hydrogen Evolution. *Appl. Catal. B Environ.* **2019**, *246*, 61–71.

[9] Chen, P. W.; Li, K.; Yu, Y. X.; Zhang, W. De. Cobalt-Doped Graphitic Carbon Nitride Photocatalysts with High Activity for Hydrogen Evolution. *Appl. Surf. Sci.* **2017**, *392*, 608–615.

[10] Wu, W.; Ruan, Z.; Li, J.; Li, Y.; Jiang, Y.; Xu, X.; Li, D.; Yuan, Y.; Lin, K. In Situ Preparation and Analysis of Bimetal Co-Doped Mesoporous Graphitic Carbon Nitride with Enhanced Photocatalytic Activity. *Nano-Micro Lett.* **2019**, *11* (1), 10.

Address correspondence to First A. Firstauthor, email1; Third C. Thirdauthor, email2